Effects of swimming environment on bacterial motility 5 50

Cite as: Phys. Fluids **34**, 031907 (2022); https://doi.org/10.1063/5.0082768 Submitted: 18 December 2021 • Accepted: 15 February 2022 • Published Online: 09 March 2022

🧓 Dokyum Kim (김도겸), 🗓 Yongsam Kim (김영삼) and 🗓 Sookkyung Lim (임숙경)

COLLECTIONS

- F This paper was selected as Featured
- SC) This paper was selected as Scilight







ARTICLES YOU MAY BE INTERESTED IN

The third golden age of aeroacoustics

Physics of Fluids 34, 031301 (2022); https://doi.org/10.1063/5.0084060

A novel computational approach to simulate microswimmers propelled by bacterial flagella Physics of Fluids 33, 111903 (2021); https://doi.org/10.1063/5.0069343

Bacteria change their swimming patterns based on their environment Scilight 2022, 101104 (2022); https://doi.org/10.1063/10.0009818

APL Machine Learning

Open, quality research for the networking communities

MEET OUR NEW EDITOR-IN-CHIEF



Effects of swimming environment on bacterial motility (5) (6)

Cite as: Phys. Fluids **34**, 031907 (2022); doi: 10.1063/5.0082768 Submitted: 18 December 2021 · Accepted: 15 February 2022 · Published Online: 9 March 2022







Dokyum Kim (김도겸), 👝 Yongsam Kim (김영삼), 🗀 🕞 and Sookkyung Lim (임숙경) 🖰 🕞

AFFILIATIONS

- ¹Department of Mathematics, Chung-Ang University, Dongjakgu, Heukseokdong, Seoul 156-756, Republic of Korea
- ²Department of Mathematical Sciences, University of Cincinnati, 4199 French Hall West, Cincinnati, Ohio 45221, USA

ABSTRACT

Swimming trajectories of bacteria can be altered by environmental conditions, such as background flow and physical barriers, that limit the free swimming of bacteria. We present a comprehensive model of a bacterium that consists of a rod-shaped cell body and a flagellum which is composed of a motor, a hook, and a filament. The elastic flagellum is modeled based on the Kirchhoff rod theory, the cell body is considered to be a rigid body, and the hydrodynamic interaction of a bacterium near a wall is described by regularized Stokeslet formulation combined with the image system. We consider three environmental conditions: (1) a rigid surface is placed horizontally and there is no shear flow, (2) a shear fluid flow is present and the bacterium is near the rigid surface, and (3) while the bacterium is near the rigid surface and is under shear flow, an additional sidewall which is perpendicular to the rigid surface is placed. Each environmental state modifies the swimming behavior. For the first condition, there are two modes of motility, trap and escape, whether the bacterium stays near the surface or moves away from the surface as we vary the physical and geometrical properties of the model bacterium. For the second condition, there exists a threshold of shear rate that classifies the motion into two types of paths in which the bacterium takes either a periodic coil trajectory or a linear trajectory. For the last condition, the bacterium takes upstream motility along the sidewall for lower shear rates and downstream motility for larger shear flow rates.

Published under an exclusive license by AIP Publishing. https://doi.org/10.1063/5.0082768

I. INTRODUCTION

In the microbial world, many species of bacteria utilize their flagellar rotation for propulsion in fluids to search for nutrients or repel themselves from harmful substances. Motility of flagellated bacteria can be altered by the surrounding physical and chemical environments. When there are no physical barriers or chemical stimuli, a bacterium *E. coli*, for example, runs approximately straight by a flagellar bundle with all motors turning counterclockwise (CCW) and all flagella forming left-handed helices. However, *E. coli* draws a circular trajectory when located near a solid surface, which allows the cell to be confined close to the surface. However, are entrapped near a rigid surface may become the onset of biofilm formation that is responsible for many microbial infection.

Bacterial motility near a planar wall has been studied using a mathematical theory of an infinite waving sheet as the swimmer, ¹² boundary element method, ^{7,13–15} a far-field theory, ^{16,17} and resistive force theory. ¹⁸ However, the flagellum in the previous studies was modeled as a rigid body that can rotate as a whole unlike the actual elastic flagellum. ^{19–22} Recently, Park *et al.* ^{23,24} presented a model of a

single-flagellated bacterium that is composed of a rigid cell body in the shape of a spheroid and an elastic flagellar filament, while a short hook that links the rotary motor and the helical filament was still missing. The compliant hook is known to play an important role in bacterial swimming. ^{1,15,25,26} In particular, Shum *et al.* ¹⁵ and Riley *et al.* ²⁶ showed computationally and theoretically that there are constraints for the rigidity of the hook in order to produce the systemic bacterial swimming observed in nature.

It is well known that dynamic fluid environments can affect the bacterial motility and thus affect microbial processes, such as nutrient uptake and biofilm formation.^{27–34} Swimming bacteria naturally have to respond to external fluid flow, and their hydrodynamic interaction with the flow determines their ability to navigate complex environments. Bacteria reorient with respect to the background flow within complex environments and may result in various trajectories, such as downstream and upstream or move toward one side, which is not well understood. Understanding of bacterial dynamics in shear flow within complex environments is important for human health issues related to microorganisms, such as pathogen transport, infections, and medical

a) Author to whom correspondence should be addressed: kimy@cau.ac.kr

device contamination. For example, it was experimentally observed that a moderate shear flow sometimes causes upstream motility (i.e., positive rheotaxis) in a flow channel, 19,35–38 which can affect bacterial transport in biomedical settings, such as the urinary tract and catheters.

The study on microswimmers in shear flow was initiated by Jeffery³⁹ about a century ago based on simple passive particle dynamics in shear flow, which was later completed by Bretherton. ⁴⁰ For active particles representing motile microorganisms, Zöttl *et al.* ^{41,42} studied the hydrodynamics of spherical and prolate squirmers in Poiseuille flow for different flow geometries and identified motions of periodic swinging and tumbling in which the frequency depends on the aspect ratio of the spheroid. This was later confirmed experimentally by Junot *et al.* using 3D Lagrangian tracking technique for motile *E. coli.* ⁴³ Marcos *et al.* ⁴⁴ demonstrated about a decade ago that bacteria *Bacillus subtilis* can exhibit rheotaxis in bulk fluid that may result from the interplay between shear flow, flagellar chirality and bacterial motility, which was further investigated by Jing *et al.* using *E. coli* bacteria in a wide channel. ³⁴ They verified experimentally and theoretically the chirality-induced rheotaxis in a bulk shear flow.

Bacterial motility in shear flow near a solid surface has been studied experimentally; in particular, it is reported that motile *E. coli* bacteria swim upstream against flow over a surface. ^{35–37,45} Recently, some scientists utilized self-propelled active nanorods representing swimming bacteria to study experimentally and computationally upstreaming motility in microfluidic channels. ^{46,47} Bacterial motility in shear flow in confined environments has attracted many scientists; however, it is still poorly understood.

In this paper, we extend the model in Ref. 24 and build a computational model based on a real bacterium. Whereas the model in Ref. 24 uses a spherical or ellipsoidal cell body without a hook, our present model is composed of a rod-shaped cell body and a complete assembly of a flagellum that incorporates a compliant hook, which is more flexible than the elastic filament. The elastic flagellum in this work is assembled with three parts in the following order: a rotary motor embedded in the cell membrane, a short compliant hook, and a long helical filament. The rotary motor generates the torque to drive the

rotation of the elastic flagellum and hence the cell body counterrotates to balance the torque. Our complete model of a bacterium may lead to understanding of the detailed hydrodynamics of bacteria in the presence of shear flow or physical barriers, such as solid surfaces.

II. MATHEMATICAL MODEL

The mathematical model of a single-flagellated bacterium consists of a cell body in the shape of a cylinder with a hemispherical cap at each end of the tube, and a helical flagellum that is attached to the cell body through a flexible, straight hook, see Fig. 1. We use the penalty method to model the cell body as a rigid body^{23,48} and describe the elastic flagellum using Kirchhoff rod theory.⁴⁹ The hydrodynamic interaction of the bacterium is described by the regularized Stokeslet formulation⁵⁰ together with the image system in order to account for the effect of a planar wall on the cell motility.^{51,52}

In the cell body dynamics, the penalty method introduced by Kim and Peskin 48,53 allows the rigid cell body to interact with a surrounding fluid. The surface of the cell body is represented by two Lagrangian descriptions, $\mathbf{X}_b(q,r,t)$ and $\mathbf{Y}_b(q,r,t)$ where t is time. The parameter pair (q,r) is Lagrangian coordinates which labels a material point of the surface of cell body. In practice, it is unlikely to keep the global Lagrangian coordinates tracking the cell body during the simulation so $\mathbf{X}_b(q,r,t)$ and $\mathbf{Y}_b(q,r,t)$ are used just for the representation purpose. The former description has no mass but the latter one carries all of the mass, and they are correspondingly linked by a system of stiff springs. Since these two descriptions are supposed to represent the same body, if there is a gap between the two corresponding boundary points, we enforce them to stay close together by applying the following restoring force density:

$$\mathbf{F}_{b}(q, r, t) = K_{b}(\mathbf{Y}_{b}(q, r, t) - \mathbf{X}_{b}(q, r, t)),$$
 (1)

where K_b is a sufficiently large constant. The restoring force $\mathbf{F}_b(q,r,t)\,dq\,dr$ is applied to the fluid by the patch of cell boundary $dq\,dr$, and the negative force $-\mathbf{F}_b\,dq\,dr$ acts on the rigid body \mathbf{Y}_b by the Newton's third law.

To describe the motion of the rigid cell body, we express $\mathbf{Y}_{\mathrm{b}}(q,r,t)$ as

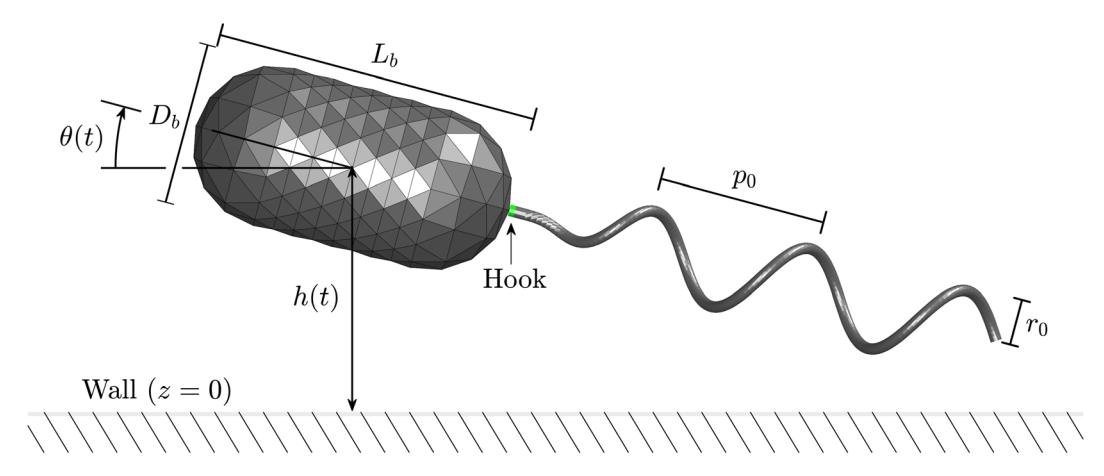


FIG. 1. Model of a single-flagellated bacterium near a rigid planar wall z = 0. The flagellum of a helical curve with pitch p_0 and radius r_0 is connected through a straight hook to the cell body of a rod shape with the length L_b and diameter D_b . The hook and the cell body share the motor in between. The distance between the center of the cell body and the wall is denoted by h(t), and the inclination angle between the major axis of the cell body (\mathbf{E}_3) and the plane z = 0 is denoted by $\theta(t)$ at time t.

$$\mathbf{Y}_{b}(q, r, t) = \mathbf{Y}_{cm}(t) + \mathcal{E}(t)\mathbf{C}(q, r), \tag{2}$$

where $\mathbf{Y}_{\rm cm}(t)$ is the center of mass of the cell body, and $\mathscr{E}(t)$ is a 3×3 matrix of which the i-th column is the i-th orthnormal basis $\mathbf{E}_i(t)$, i=1,2, and 3, for the coordinate system fixed to the body with its origin at $\mathbf{Y}_{\rm cm}(t)$. The time-independent constant vector $\mathbf{C}(q,r)$ is a 3×1 vector, which represents the coordinates fixed to the cell body in this system. Then, the equations of motion for the rigid cell body $\mathbf{Y}_{\rm b}(q,r,t)$ are now given by

$$\frac{d\mathbf{Y}_{\rm cm}}{dt} = \mathbf{V}_{\rm cm}(t), M \frac{d\mathbf{V}_{\rm cm}}{dt} = - \iint_{\Gamma} \mathbf{F}_{\rm b}(q, r, t) \, dq \, dr, \tag{3}$$

$$\frac{d\mathbf{L}}{dt} = \left[\int_{\Gamma} (\mathbf{Y}_{b}(q, r, t) - \mathbf{Y}_{cm}(t)) \times (-\mathbf{F}_{b}(q, r, t)) \, dq \, dr, \right]$$
(4)

$$\Omega(t) = \mathcal{E}(t) I_0^{-1} \mathcal{E}(t)^T \mathbf{L}(t), \frac{d\mathbf{E}_i}{dt} = \Omega(t) \times \mathbf{E}_i(t), \quad i = 1, 2, 3, \quad (5)$$

where $V_{cm}(t)$, L(t), and $\Omega(t)$ are the velocity of the center of mass, the angular momentum, and the angular velocity of the cell body, respectively. The total mass M and the initial moment of inertial tensor I_0 of the surface of the cell body can be computed by $M = \iint_{\Gamma} m(q,r) dq dr$ and $I_0 = \iint_{\Gamma} m(q,r) (\mathbf{C}^T \mathbf{C} I_3 - \mathbf{C} \mathbf{C}^T) dq dr$, respectively, where m(q,r) is the mass density and I_3 is 3×3 identity matrix. In summary, the cell body translates by Eq. (3) and rotates by Eqs. (4) and (5) at the cost of the resultant forces and moments from the deviation of two Lagrangian descriptions for the cell body.

Kirchhoff rod theory models an elastic rod as a space curve $\mathbf{X}(s,t)$ representing the centerline of the rod and an associated orthonormal triad $\{\mathbf{D}^1(s,t),\mathbf{D}^2(s,t),\mathbf{D}^3(s,t),\}$, which measures the amount of bending and twisting of the flagellum. The initial shape of our flagellum model is a tapered helical curve with a helical radius decreasing to be zero in the hook and is described by ⁵⁴

$$\mathbf{X}(s,0) = (r(s)\cos{(\alpha s)}, r(s)\sin{(\alpha s)}, s), \tag{6}$$

where α is the wave number and the helical radius r(s) is a variable function defined as

$$r(s) = \begin{cases} 0 & 0 \le s \le L_{\rm h}, \\ r_0 \left(1 - e^{-k(s - L_{\rm h})^2}\right) & L_{\rm h} \le s \le L_{\rm h} + L_{\rm f}, \end{cases}$$
 (7)

where $L_{\rm h}$ and $L_{\rm f}$ are the lengths of the hook and the helical filament, respectively, and k is a constant. The helical radius is 0 for the hook $(0 \le s \le L_{\rm h})$, which is a straight rod and then increases gradually to be r_0 for the helical filament $(L_{\rm h} \le s \le L_{\rm h} + L_{\rm f})$. Then, the vector $\mathbf{D}^3(s,0)$ is initially chosen as a unit tangent vector to the curve $\mathbf{X}(s,0)$ in Eq. (6), and the other two vectors, $\mathbf{D}^1(s,0)$ and $\mathbf{D}^2(s,0)$, are normal and binormal vectors, respectively.

The initial configuration of the centerline and the triad of the flagellum is in the equilibrium state in the absence of external forces; however, its deformation gives rise to the following internal force $\mathbf{F}(s,t)$ and moment $\mathbf{N}(s,t)$ transmitted across a section of the rod at the Lagrangian coordinate s at time t,

$$\mathbf{F} = \sum_{i=1}^{3} F_i \mathbf{D}^i, \quad \mathbf{N} = \sum_{i=1}^{3} N_i \mathbf{D}^i, \tag{8}$$

(9)

$$F_i = b_i \left(\mathbf{D}^i \cdot \frac{\partial \mathbf{X}}{\partial s} - \delta_{3i} \right), \quad N_i = a_i \left(\frac{\partial \mathbf{D}^j}{\partial s} \cdot \mathbf{D}^k - \Omega_i \right), \quad i = 1, 2, 3,$$

where δ_{3i} is the Kronecker delta, and (i,j,k) is any cyclic permutation of (1,2,3). The coefficients a_1 and a_2 are the bending moduli, a_3 is the twist modulus of the rod, b_1 and b_2 are the shear moduli, and b_3 is the stretching modulus. The strain twist vector $(\Omega_1, \Omega_2, \Omega_3)$ designates the intrinsic property of the helical rod in which $\kappa \equiv \sqrt{\Omega_1^2 + \Omega_2^2}$ is the intrinsic curvature and Ω_3 is the intrinsic twist of the flagellum of which the sign determines the helical handedness of the rod.

Let $\mathbf{u}(\mathbf{x}, t)$ and $p(\mathbf{x}, t)$ be the fluid velocity and pressure, respectively, where \mathbf{x} is the fixed Cartesian coordinates and t is the time. Then, the coupled system of equations that describes the hydrodynamics of a bacterium in a viscous incompressible fluid is given as follows:

$$0 = -\nabla p + \mu \Delta \mathbf{u} + \mathbf{g}, \quad 0 = \nabla \cdot \mathbf{u},$$

$$\mathbf{g}(\mathbf{x}, t) = \int \mathbf{F}_{b}(q, r, t) \psi_{\epsilon}(\mathbf{x} - \mathbf{X}_{b}(q, r, t)) \, dq \, dr$$

$$+ \int_{0}^{L} (-\mathbf{f}(s, t)) \psi_{\epsilon}(\mathbf{x} - \mathbf{X}(s, t)) \, ds + \frac{1}{2} \nabla$$

$$\times \int_{0}^{L} (-\mathbf{n}(s, t)) \psi_{\epsilon}(\mathbf{x} - \mathbf{X}(s, t)) \, ds,$$
(11)

$$0 = \mathbf{f} + \frac{\partial \mathbf{F}}{\partial s}, \quad 0 = \mathbf{n} + \frac{\partial \mathbf{N}}{\partial s} + \left(\frac{\partial \mathbf{X}}{\partial s} \times \mathbf{F}\right), \tag{12}$$

$$\frac{\partial \mathbf{X}(s,t)}{\partial t} = \mathbf{u}(\mathbf{X}(s,t),t), \quad \frac{\partial \mathbf{X}_{b}(q,r,t)}{\partial t} = \mathbf{u}(\mathbf{X}_{b}(q,r,t),t), \quad (13)$$

$$\frac{\partial \mathbf{D}^{i}(s,t)}{\partial t} = \mathbf{w}(\mathbf{X}(s,t),t) \times \mathbf{D}^{i}(s,t), \quad i = 1, 2, 3,$$
 (14)

$$\mathbf{w}(\mathbf{x},t) = \frac{1}{2}\nabla \times \mathbf{u}(\mathbf{x},t). \tag{15}$$

Equation (10) is the incompressible Stokes equations where μ is the fluid viscosity. The external force density ${\bf g}$ in Eq. (11) consists of three parts; the penalty spring force from the cell body in the first term and the contribution from the elastic flagellum in the last two terms in which ${\bf f}$ and ${\bf n}$ are the force and torque densities applied by the fluid on the flagellum, respectively. We assume in the present work that the flagellum is neutrally buoyant and the inertia of the flagellum is neglected. Thus, Eq. (12) expresses the equations for force and torque balances on the flagellum. The radially symmetric blob function ψ_{ϵ} in Eq. (11) is defined as

$$\psi_{\epsilon}(\mathbf{r}) = \frac{15\epsilon^4}{8\pi(|\mathbf{r}|^2 + \epsilon^2)^{7/2}},\tag{16}$$

where ϵ is the regularization parameter and $\mathbf{r}=\mathbf{x}-\mathbf{X}$ for a point \mathbf{x} in the fluid. The blob function ψ_{ϵ} is a bell-shaped function with infinite support, spreading most of the force and moment within a ball with the radius ϵ and the center at the point \mathbf{X} and satisfying $\iiint_{\mathbb{R}^3} \psi_{\epsilon}(\mathbf{r}) \, d\mathbf{r} = 1.^{50,55}$

The motion of the immersed boundaries, the flagellum X and the cell body X_b , is described in Eq. (13), which expresses the no-slip condition for the linear velocity. Equation (14) states that the triads associated with the flagellum rotate at the local angular velocity of the fluid (half the vorticity field) defined in Eq. (15). Equations similar to these are derived and discussed in Refs. 49 and 50.

The bottom end X(0, t) of the flagellum is assigned to the motor point attached to one pole of the cell body denoted as $Y_b^0(t)$. In reality,

they are physically the same point and move in time together as the cell swims. To incorporate this into our model, we connect $\mathbf{X}(0,t)$ to $\mathbf{Y}_{\mathrm{b}}^{0}(t)$ and align the vector $\mathbf{D}^{3}(0,t)$, which is approximately tangent to the flagellum at $\mathbf{X}(0,t)$, with the normal vector to the surface of the cell body at $\mathbf{Y}_{\mathrm{b}}^{0}(t)$. This is done by defining the feedback force and moment densities as follows:

$$\mathbf{f}_{\rm m}(t) = K_{\rm m}^{1}(\mathbf{Y}_{\rm b}^{0}(t) - \mathbf{X}(0, t)), \tag{17}$$

$$\mathbf{n}_{\rm m}(t) = K_{\rm m}^2(\mathbf{D}^3(0,t) \times \mathbf{E}_3(t)),$$
 (18)

where $K_{\rm m}^1$ and $K_{\rm m}^2$ are large constants. Then the force density ${\bf f}_{\rm m}(t)$ is added to the force density ${\bf f}$ in Eq. (12) at the bottom end point of the hook ${\bf X}(0,t)$, the negative force density $-{\bf f}_{\rm m}(t)$ is added to ${\bf F}_{\rm b}(q,r,t)$ at ${\bf Y}_{\rm b}^0(t)$ and affects the total force and torque on the cell body. Similarly, the moment density ${\bf n}_{\rm m}(t)$ is added to the moment ${\bf n}$ in Eq. (8) at ${\bf X}(0,t)$, and the negative moment $-{\bf n}_{\rm m}(t)$ is added to the total torque ${\bf T}(t)$ on the cell body.

The motor of the flagellum rotates at any given frequency f about the tangent vector $\mathbf{D}^3(0, t)$. This can be done by prescribing the orthonormal triad at the motor point $\mathbf{X}(0, t)$ as follows:

$$\mathbf{D}^{i}(0,t) = \mathcal{R}(\mathbf{D}^{3}(0,t))\mathbf{D}_{\text{mot}}^{i}(0,t), \quad i = 1, 2,$$
(19)

where $\mathcal{B}(\mathbf{D}^3(0,t))$ is a rotational matrix to transform the unit vector (0, 0, 1) to the unit vector $\mathbf{D}^3(0,t)$. The two orthonormal vectors $\mathbf{D}^i_{\mathrm{mot}}(t), \ i=1,2$ represent the vectors which are rotated at frequency f from the two standard basis (1,0,0) and (0,1,0), respectively,

$$\mathbf{D}_{\text{mot}}^{1}(t) = (\cos{(2\pi f t)}, \sin{(2\pi f t)}, 0), \mathbf{D}_{\text{mot}}^{2}(t) = (-\sin{(2\pi f t)}, \cos{(2\pi f t)}, 0).$$

The rotary motor generates a twist that is transmitted along the flagellum to its free end, which leads to the rotation of the helical filament, and the resultant countertorque at the rotating motor automatically appears to balance the torque on the cell body so that the cell body counter-rotates. See Ref. 23 for a more detailed description of mathematical formulation.

The hydrodynamic interaction between fluid and the bacterium including the effect of a planar wall is described by the regularized Stokeslet formulation combined with the image system. 51,52 We consider an infinite plane wall (z = 0) at which the fluid velocity vanishes. In the presence of the external force g resulting from the forces and toques of the immersed boundaries (flagellum and cell body), the solution (the linear velocity) of Eq. (10) may not be zero on the wall. The idea of the method of image system is to define various fundamental solutions (kernels), such as Stokeslet, potential dipole, rotlet, doublet, quadrupole, and rotlet doublet, and to apply them to appropriate forces and torques at the image points of the immersed boundaries so that the flow at the wall is at rest. The image system method was introduced by Cortez et al. 51,52 in order to apply the no-slip wall conditions for the linear and angular velocities. See Ref. 24 for the detailed derivation of the mathematical formulation and the numerical schemes which were applied to a bacterial locomotion near the planar wall

The regularized Stokeslet formulation is a Lagrangian (meshfree) method which is based on the superposition of exact solutions of Stokes equations when forces and moments are given as regularized functions at material points in a fluid. Thus, we need to discretize the flagellum and the cell body surface only without a mesh for the fluid domain. In our simulations, the flagellum is reparametrized by arc length before being used and is discretized with equal meshwidth $\Delta s=0.035\,\mu{\rm m}$ along the curve. The cell body is represented by a triangulated surface composed of Lagrangian markers with the average area $\Delta A_b=0.0041\,\mu{\rm m}^2$ of the triangles, see Table I.

The accuracy of the Lagrangian method depends on the mesh size and the regularization parameter ϵ , and the error was proved and validated numerically to be $\mathcal{O}(\Delta s^2/\epsilon^3) + \mathcal{O}(\Delta A_b/\epsilon^3) + \mathcal{O}(\epsilon)$, where the former two terms are the quadrature (discretization) error for Eq. (11) and the latter one is the regularization error. Even though the regularized Stokeslet formulation with the image system has no such theory for the accuracy, it was validated by comparing the drag force computed by the regularized image system with the analytical value of drag force generated on a sphere moving near a wall in Ref. 51 and by comparing the swimming motions of a bacteria near wall computed using the present method and using a traditional target point idea for a fixed wall in Ref. 24.

III. RESULTS AND DISCUSSION

We investigate the swimming motion of a single-flagellated bacterium placed near a planar wall in the absence of a shear flow first and then in the presence of a shear flow. Figure 1 shows a schematic diagram of our computational model in which h(t) is the distance of the center of the cell body from the wall, and $\theta(t)$ is the inclination angle of the cell body from the wall z=0 at time t. Table I shows the computational and physical parameters for the prototypical bacterium model used in this work;^{2,3} however, we vary the initial settings, such as the height and the inclination angle, the geometrical properties of the flagellum and the cell body, and the elastic and geometrical properties of the hook to see the dynamical effect of these variations. In the

TABLE I. Computational and physical parameters.

Parameters (symbol)	Value
Fluid viscosity (μ)	10 ⁻⁶ g/(μm⋅ s)
Regularization parameter (ϵ)	$3\Delta s$
Time step (Δt)	$5.0 \times 10^{-8} \text{ s}$
Meshwidth for flagellum (Δs)	$0.035~\mu\mathrm{m}$
Helical radius of filament (r_0)	$0.2~\mu\mathrm{m}$
Helical pitch of filament (p_0)	$2.0~\mu\mathrm{m}$
Number of helical turns (N_{λ})	3.5
Bending modulus of filament ($a_1 = a_2$)	$0.007 \text{ g} \mu\text{m}^3/\text{ s}^2$
Twist modulus of filament (a_3)	$0.007 \mathrm{g} \mu\mathrm{m}^3/\mathrm{s}^2$
Shear modulus ($b_1 = b_2$)	$2.0 \mathrm{g} \;\mu\mathrm{m}/\;\mathrm{s}^2$
Stretch modulus (b_3)	$2.0 \mathrm{g}\mu\mathrm{m}/\mathrm{s}^2$
Length of hook (L_h)	$2\Delta s$
Bending modulus of hook ($a_1^{\text{hook}} = a_2^{\text{hook}}$)	$0.000 175 \mathrm{g} \mu \mathrm{m}^3 / \mathrm{s}^2$
Twist modulus of hook (a_3^{hook})	$0.007 \mathrm{g}\mu\mathrm{m}^3/\mathrm{s}^2$
Rotation rate of motor (<i>f</i>)	100.0 Hz
Cell body length (L_b)	$2.0~\mu\mathrm{m}$
Cell body diameter (D_b)	$1.0~\mu\mathrm{m}$
Cell body density (<i>m</i>)	$10^{-12} \mathrm{g/\mu m^2}$
Average area of triangles (ΔA_b)	$0.0041 \mu \text{m}^2$

absence of the shear flow, we are particularly interested in the critical values of some of these parameters which categorize the motions into two groups, *trapping* motion and *escaping* motion, in which the cell stays near the wall or moves away from the wall, respectively. In the presence of the shear flow, we investigate how shear flow alters trajectories of bacteria. We also investigate the effect of an additional sidewall on the dynamical motion of bacteria under the shear flow.

A. Dynamical motion of a bacterium near a solid planar wall

In the absence of physical barriers or chemical stimuli in fluid, the CCW rotation of the motor induces the CCW rotation of the left-handed flagellum that leads the cell to a straightforward run, while the cell body counter-rotates to balance the torque. When the cell is placed near a solid wall, the balance between the opposite torques on the cell body and on the rotating flagellum together with its hydrodynamic interaction with the solid wall deviates the swimming path from a straight line to a CW circle when viewed toward the wall. This has been experimentally and numerically observed. 5–7,14,18,56,57 Moreover,

the balance between a hydrodynamic attraction toward the wall due to the image singularities 58 and the repelling force from the wall gives a stable height $h^{\ast},$ which may enhance the chance of the bacterial adhesion to the surface to form biofilm. $^{8-10}$

Figure 2 (Multimedia view) shows time evolution of locomotion of the prototypical bacterium when the initial height and inclination angle are set as $h_0=3.0\mu\mathrm{m}$ and $\theta_0=0$, respectively. Parameter values for this simulation are shown in Table I. Two main features are observed from the swimming trajectory: the model organism swims toward the wall and eventually stays at a certain height level as shown in (a), and the bacterium draws a CW circular trajectory with an approximately constant radius as shown in (b).

To describe the swimming pattern quantitatively, we measure the height h(t) (c), the radius R(t) of curvature of the trajectory (d), the forward swimming speed $V_f(t)$ (e), and the inclination angle $\theta(t)$ (f) as functions of time for various initial heights h_0 . Here the forward swimming speed is defined as $V_f(t) = \mathbf{V}_{\rm cm}(t) \cdot \mathbf{E}_3(t)$ where $\mathbf{E}_3(t)$ is the unit vector from the motor point to the opposite node of the cell body, and the radius R(t) of the trajectory is defined as the reciprocal of the local curvature of the trajectory at time t. The limiting values of

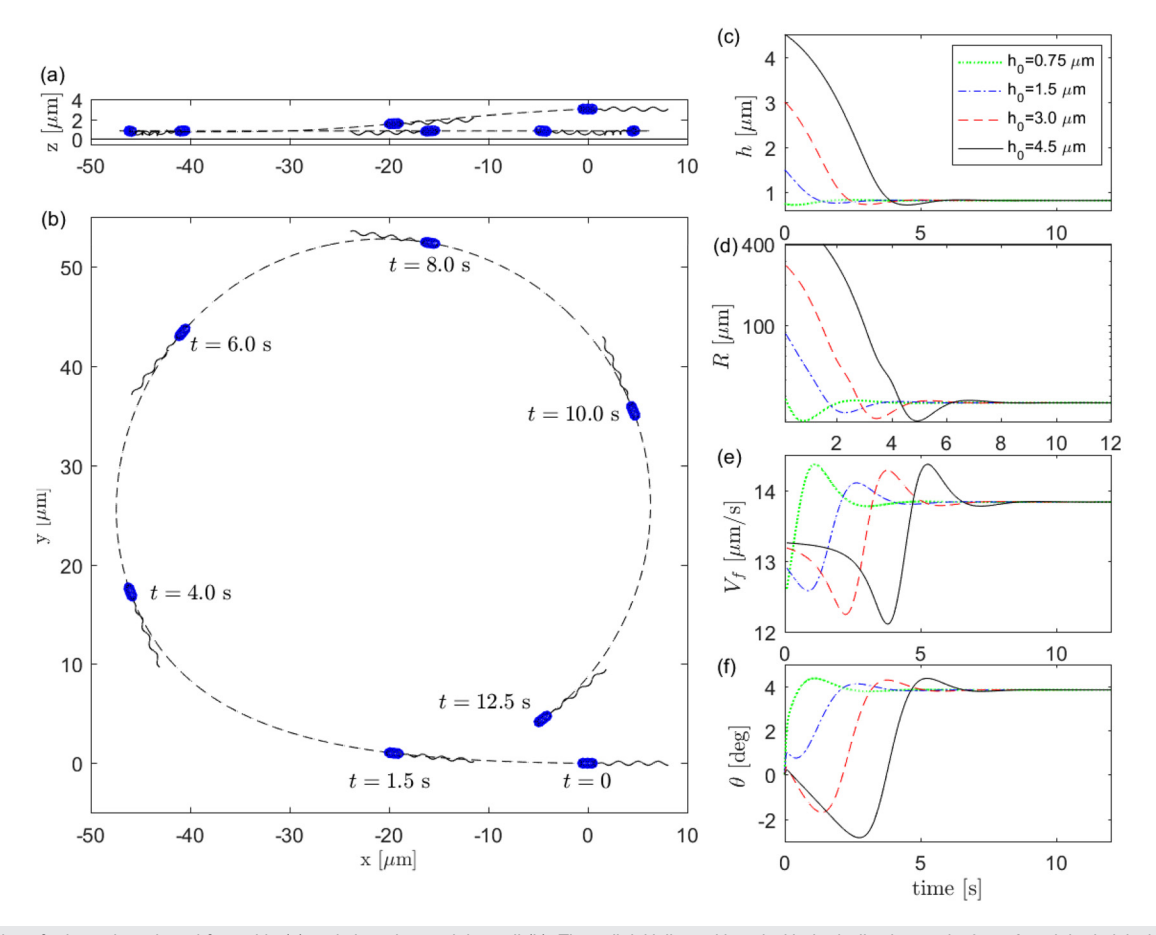


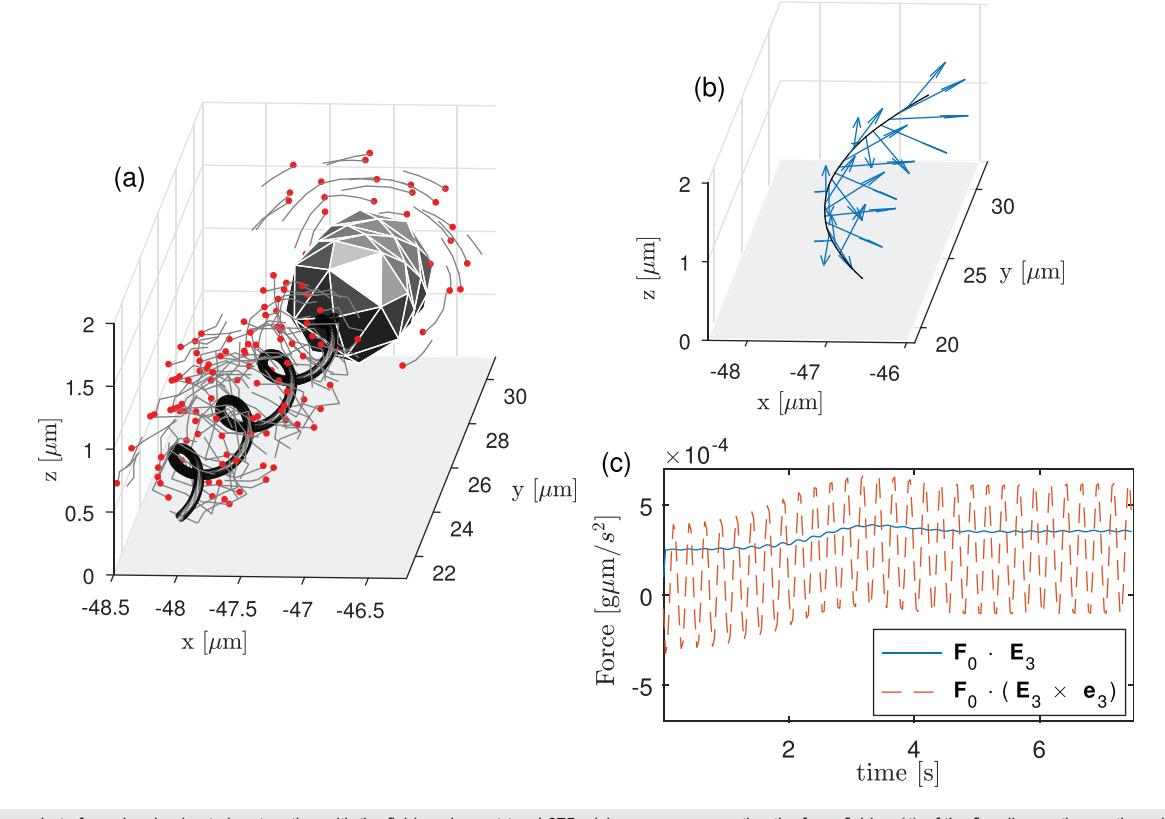
FIG. 2. Motion of a bacterium viewed from side (a) and viewed toward the wall (b). The cell, initially positioned with the inclination angle $\theta_0=0$ and the height $h_0=3.0\,\mu\text{m}$, swims toward the wall and follows a circular trajectory. Parameter values for this simulation are displayed in Table I. The right column displays time evolutions of the height h(t) (c), the radius R(t) of curvature of the trajectory (d), the forward swimming speed $V_f(t)$ (e), and the inclination angle $\theta(t)$ (f) for various initial heights h_0 of $h_0=0.75\,\mu\text{m}$ (dotted), 1.5 μm (dash-dotted), 3.0 μm (dashed), and 4.5 μm (solid). Multimedia view: https://doi.org/10.1063/5.0082768.1

these four measurements are shown to be independent of the initial height with $h_0=0.75,\,1.5,\,3.0,\,$ and 4.5 in micrometers, and the limiting values are $h^*=0.824\,\mu\mathrm{m},\,R^*=26.8\,\mu\mathrm{m},\,V_f^*=13.83\,\mu\mathrm{m/s},\,$ and $\theta^*=3.84^\circ.$ When the initial height h_0 is large (larger than $1.5\,\mu\mathrm{m}),\,$ the cell body moves downward and the inclination angle $\theta(t)$ decreases for some time with the negative sign, which implies that the cell body points toward the wall. When the cell body gets close to the wall, the angle $\theta(t)$ turns to increase and becomes a positive value, which indicates that the cell body points away from the wall. Note that the limiting value θ^* is positive so as to balance the attractive force of near-wall bacteria and the lift force on the moving cell body. 14

Figure 3 shows a snapshot of a swimming bacterium together with the fluid markers at t=4.875 s (a), arrows representing the force field $\mathbf{F}_0(t)$ of the flagellum acting on the cell body along the trajectory of cell body center $\mathbf{Y}_{cm}(t)$ from t=4.0 s to 5.375 s (b), and time evolution of two components of the force $\mathbf{F}_0(t)$, $\mathbf{F}_0(t) \cdot \mathbf{E}_3(t)$ (solid line) and $\mathbf{F}_0(t) \cdot (\mathbf{E}_3(t) \times \mathbf{e}_3)$ (dashed line) (c) in the case described in Figs. 2(a) and 2(b). Fluid markers start out near the bacterium and leave trails that show their recent trajectories. We can observe that, when viewed from the flagellum toward the cell body, the fluid markers near the cell body rotate CW, while the fluid markers near the flagellum rotate CCW moving slightly backward.

The force $\mathbf{F}_0(t)\cdot\mathbf{E}_3(t)$, which represents the forward directional component of the force $\mathbf{F}_0(t)$, gradually increases and then settles down to a positive constant value, which induces a forward directional motion of the bacterium as shown in Fig. 2(e). The force $\mathbf{F}_0(t)\cdot(\mathbf{E}_3(t)\times\mathbf{e}_3)$, where \mathbf{e}_3 is the positive z-directional unit vector, represents the centripetal directional component of force $\mathbf{F}_0(t)$ along the circular swimming trajectory. While the centripetal directional force goes through a large-amplitude oscillation, it settles down to a stable oscillation with a positive average value, which, together with the positive forward directional force, induces a CW circular swimming trajectory as shown in Fig. 2(b).

Figure 2 demonstrates that when a cell is initially placed close enough to the wall and the major axis of the cell is parallel to the wall, the cell is confined in a trapping zone. However, if bacteria are initially placed far away from the wall and/or has a large positive inclination angle, they might stay away from the trapping zone and reside in the escaping zone. Figure 4 shows time evolutions of the height h(t) (a), the radius R(t) of curvature of the trajectory (b), the forward swimming speed $V_f(t)$ (c), and the inclination angle $\theta(t)$ (d) as functions of time for different combinations of initial height h_0 and inclination angle θ_0 . The model bacterium is of the prototype, and the motor rotates at f=100 Hz. When $h_0=3.0~\mu{\rm m}$ and $\theta_0=10^\circ$ (lines with +) or $h_0=2.3~\mu{\rm m}$ and $\theta_0=15^\circ$ (lines with $^\circ$), the bacterium gets close



 $\textbf{FIG. 3}. \ \, \text{A snapshot of a swimming bacterium together with the fluid markers at $t=4.875$ s (a), arrows representing the force field $\mathbf{F}_0(t)$ of the flagellum acting on the cell body along the trajectory of cell body center $\mathbf{Y}_{cm}(t)$ from $t=4.0$ to 5.375$ s (b), and time evolution of two components of the force $\mathbf{F}_0(t)$, $\mathbf{F}_0(t)$ \cdot $\mathbf{E}_3(t)$ (solid line) and $\mathbf{F}_0(t)$ \cdot $(\mathbf{E}_3(t) \times \mathbf{e}_3)$ (dashed line) (c) in the case described in $\mathbf{Figs.}$ 2(a) and 2(b). Fluid markers start out near the bacterium and leave trails that show their recent trajectories. The forces $\mathbf{F}_0(t)$ \cdot $\mathbf{E}_3(t)$ and $\mathbf{F}_0(t)$ \cdot $(\mathbf{E}_3(t) \times \mathbf{e}_3)$ represent the forward directional component and the centripetal directional component, respectively, along the circular swimming trajectory. }$

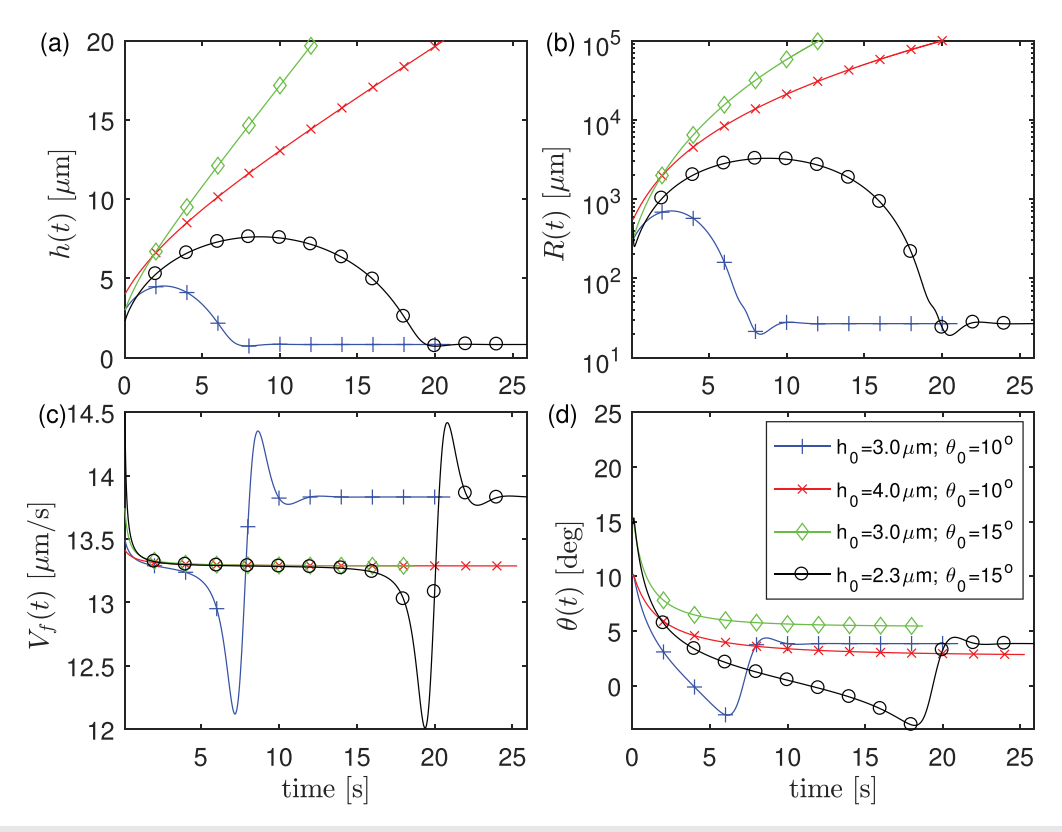


FIG. 4. Time evolutions of the height h(t) (a), the radius R(t) of curvature of the trajectory (b), the forward swimming speed $V_f(t)$ (c), and the inclination angle $\theta(t)$ (d) for different combinations of the initial height h_0 and initial inclination angle θ_0 . When both h_0 are smaller than some critical values, the bacterium gets close to the wall and moves into the trapping zone. Otherwise, the bacterium goes far away from the wall and gets into the escaping zone.

to the wall and moves into the trapping zone. However, when the height increases to $h_0=4.0~\mu\mathrm{m}$ with $\theta_0=10^\circ$ (lines with \times) or when the inclination increases to $\theta_0=15^\circ$ with $h_0=3.0~\mu\mathrm{m}$ (lines with \diamondsuit), the bacterium swims in the escaping zone, in which it moves far away from the wall [see Fig. 4(a)] and draws a trajectory of a straight line in contrast to the circular trajectory [see Fig. 4(b)].

Note that even though the bacterium in the trapping zone goes through different paths during the transient time depending on h_0 and θ_0 , all cases reach the same steady states as before. Note also that the bacterium in the escaping zone reaches the same limiting value of the forward velocity, $V_f^* = 13.29 \,\mu\text{m/s}$, see Fig. 4(c). In fact, when a bacterium is far away from the wall so that it feels no effect of the wall, it moves in a uniform direction at a uniform speed which is smaller than the speed of the bacterium near the wall, compare the limiting speeds in (c). The inclination angles of the bacterium in the escaping zone converge to different limiting values depending on h_0 and θ_0 , see Fig. 4(d).

Figure 5 displays a classification of dynamical motions of bacteria into two regions: trapping (light gray) and escaping (white) zones. We do not consider the bacterium with the initial inclination angle and height in the dark gray region at the bottom, since its flagellum passes through the wall, $z\!=\!0$, in our initial setting. The markers "×" and "o" represent the initial height and inclination angle which make the bacterium to escape and be trapped, respectively. By using these computed data and applying the least squares approximation to the

function $h(\theta) = \frac{a}{\theta - b} + c$, we construct the curve separating the θ -h plane into trapping and escaping zones. We also draw some illustrative trajectories of the bacterium which starts at various initial points (" \bullet "). The bacteria which start in the escaping zone go up higher with some convergent inclination angles depending on h_0 and θ_0 , as indicated by the dashed lines. The solid lines show that the swimming trajectories of the bacterium which starts in the trapping zone are attracted to the same steady state with $\theta^* = 3.84^\circ$ and $h^* = 0.824\mu$ m (" \bigstar ").

B. Dependence on geometrical and elastic properties of bacteria

We here investigate the dependence of the swimming patterns of bacteria near wall upon various geometrical and elastic properties of the helical flagellum, cell body, and hook. Note that, in Secs. III B, III C and III D, we express the forward swimming speed, radius of curvature of the trajectory, height, and inclination angle in the dimensionless form by scaling them with $V_0^*=13.83\,\mu\text{m/s},~R_0^*=26.8\,\mu\text{m},~h_0^*=0.824\,\mu\text{m},$ and $\theta_0^*=3.84^\circ$, respectively, which are the steady values produced with the default parameter values given in Table I.

We first investigate how the geometrical parameters of the flagellum affect its swimming course near a solid surface. We vary one parameter among number of helical turns N_{λ} , helical radius r_0 , and helical pitch p_0 of the flagellum, while the other parameters are held

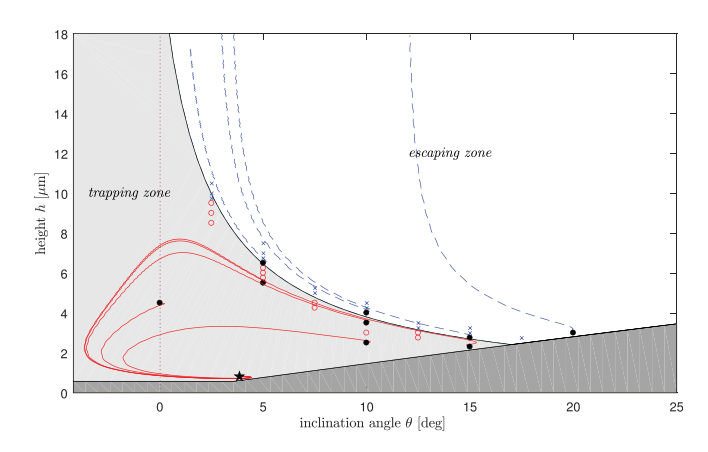


FIG. 5. Classification of dynamical behaviors depending on the initial inclination angle θ_0 and height h_0 : trapping (light gray) and escaping (white) zones. The markers "×" and "o" represent the initial height and inclination angle which make the bacterium to escape and be trapped, respectively. We do not consider the bacterium with the initial inclination angle and height in the dark gray region, since it flagellum passes through the wall in the initial setting. The dashed lines (or solid lines) represent some trajectories of bacteria which start at various initial points (\bullet) and illustrate that the bacteria starting from the escaping zone (or trapping zone) stay within the same zone. The bacteria which start in the trapping zone are attracted to the same steady state indicated by " \bigstar ."

fixed at default values; $r_0=0.2~\mu\text{m}$, $p_0=2.0~\mu\text{m}$, and $N_\lambda=3.5$. The rest of the physical parameter values are the same as in Table I, and the model bacterium is initially positioned with $h_0=1.5~\mu\text{m}$ and $\theta_0=0$. We have observed that the bacteria approach stable circular swimming paths with constant heights for certain ranges of r_0 , p_0 , and N_λ . Figure 6 shows limiting values of stable circular trajectories resulted from the changes in each of the three geometrical parameters: $N_\lambda=2, 2.5, 3, 3.5,$ and 4 (a); $r_0/D_b=0.1, 0.15, 0.2, 0.25, 0.3,$ and 0.35 (b); and $p_0/D_b=1.0, 1.5, 2.0, 2.5,$ and 3.0 (c), where $D_b=1.0~\mu\text{m}$ is the diameter of the cell body. For the change of each parameter, we display normalized limiting values of forward swimming speed V_f^*/V_0^* , radius R^*/R_0^* of the circular trajectory, height h^*/h_0^* , and inclination angle θ^*/θ_0^* .

As N_{λ} increases and thus the flagellum gets longer, the normalized forward velocity V_f^*/V_0^* and the radius R^*/R_0^* increase; however, the height h^*/h_0^* decreases, and the inclination angle θ^*/θ_0^* almost does not change, as shown in (a). When the helical radius r_0/D_b and pitch p_0/D_b increase independently, the swimming velocity V_f^*/V_0^* increases first and then decreases with the maximal values attained at $r_0/D_b = 0.3$ and pitch $p_0/D_b = 2.5$, see the first row. The limiting height h^*/h_0^* is shown to decrease when $r_0/D_b \geq 0.25$ and $p_0/D_b \geq 2.0$ (third row). While the radius R^*/R_0^* and the inclination angle θ^*/θ_0^* do not change much when the pitch varies, they change noticeably when the helical radius varies, see the second and fourth rows.

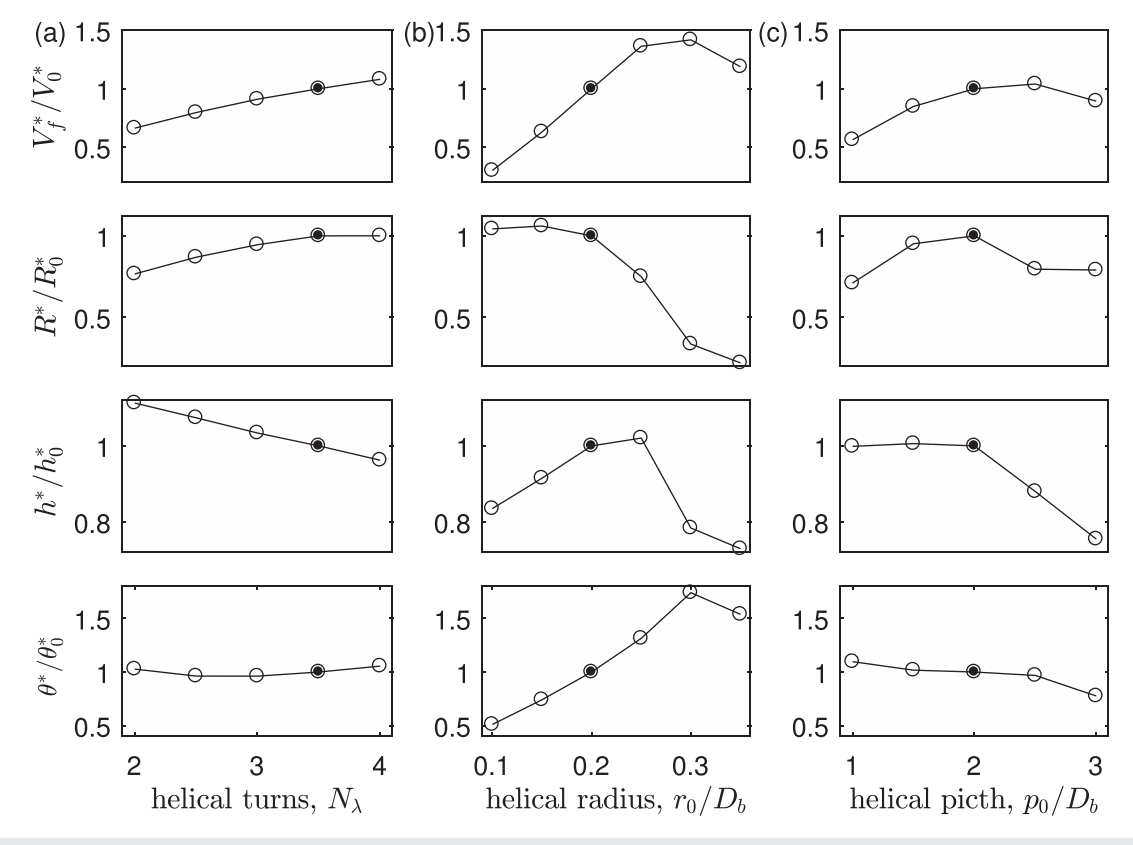


FIG. 6. Limiting values of stable circular swimming motions resulted from changes in three geometrical parameters; number of helical turns N_{λ} (a), helical radius r_0/D_b (b), and helical pitch p_0/D_b (c). For the change of each parameter, four types of normalized limiting values are displayed; forward swimming speed V_f^*/V_0^* (first row), radius R^*/R_0^* (second row) of the circular trajectory, height h^*/h_0^* (third row), and inclination angle θ^*/θ_0^* (fourth row). The filled circles represent the simulation results with the default parameter values.

In particular, as the helical radius r_0/D_b increases, the limiting value of the inclination angle θ^*/θ_0^* generally increases, whereas the limiting radius R^*/R_0^* of curvature of the trajectory tend to decrease, which was reported in Ref. 18.

The swimming pattern of bacteria near a wall is also dependent on the shape of the cell body. To see this, we start with the prototypical bacterium, which takes the parameter values given in Table I, and vary only the length of the cell body L_b with the diameter being fixed at $D_b = 1.0 \,\mu\text{m}$. It is known that, as single-flagellated cells grow, their cell bodies elongate the length while keeping the body width the same and thus the aspect ratio L_b/D_b increases. Figure 7(a) (Multimedia view) shows trajectories of bacteria with five different aspect ratios: $L_b/D_b = 1.5$, 2.0, 2.5, 3.0, and 3.5. All the bacteria are initially placed at the same location $(0,0,1.5 \,\mu\text{m})$ indicated by the filled circle, and their configurations are captured at t = 12.5 s, which are scaled up by a factor of three for a clearer view. As L_b/D_b increases, cells draw circular paths with larger radii, stay farther away from the wall, and swim slower, see Figs. 7(b)-7(d). When the aspect ratio is sufficiently large, for example, in the case of $L_b/D_b = 3.5$, the cell escapes from the trapping zone and keeps moving away from the wall in a linear manner. The threshold of the aspect ratio that separates the escaping mode from the trapping one is obtained approximately at $L_b/D_b = 3.45$, see the vertical dotted line in the second column. As L_b/D_b increases, the limiting inclination angle θ^*/θ_0^* in the trapping zone increases first and then decreases with the maximal value attained at $L_b/D_b = 3.0$. These results are consistent with those in the previous studies.

It is reported that the bacteria with a longer flagellum prone to stay near a wall unlike the bacteria with a shorter flagellum, which suggests the existence of a threshold of helical length that separates the swimming motions into trapping mode and escaping mode. 14,23 In order to investigate the cell's modes of motility depending on the geometrical properties, we consider bacteria with various helical properties and cell body lengths. Figure 8 shows the critical numbers of helical turns N_{λ} (upper panels) and the corresponding curvilinear lengths of the flagellum l_f normalized by D_b (lower panels) as functions of normalized radius r_0/D_b (a) and (d), helical pitch p_0/D_b (b) and (e), and aspect ratio L_b/D_b (c) and (f). The region above each curve indicates the trapping zone, i.e., when bacteria have a larger number of helical turns and thus a longer length of the flagellum than those given on the curve, they stay in the trapping zone. The filled circles represent the simulation results with the default values. The critical number of helical turns and the flagellum length are inversely proportional to the pitch shown in (b) and (e) and is proportional to the aspect ratio shown in (c) and (f), see also Ref. 24. It is interesting to see from (a) that the critical number of helical turns is almost independent of the helical radius; however, the critical value of curvilinear length of the flagellum increases as the helical radius increases for the model organism to stay in the trapping zone.

The swimming dynamics of bacteria can also be influenced by the geometrical and elastic properties of the hook. So far, we have used the straight hook with the length $L_{\rm h}=2$ $\Delta s=0.07$ $\mu {\rm m}$ and the bending modulus $a_1^{\rm hook}=a_2^{\rm hook}=0.000$ 175 g $\mu {\rm m}^3/{\rm s}^2$, which is 40 times smaller than that of the flagellum, i.e., $a_1^{\rm hook}=a_1/40$. The twist moduli of the hook and the flagellum remain the same. Here, we investigate the dynamics of bacteria with (1) various lengths of the hook from Δ to 5 Δ s with the bending modulus of the hook being fixed at $a_1^{\rm hook}$ and with (2) various bending moduli $a_1^{\rm hook}$ of the hook from $a_1/120$ to a_1

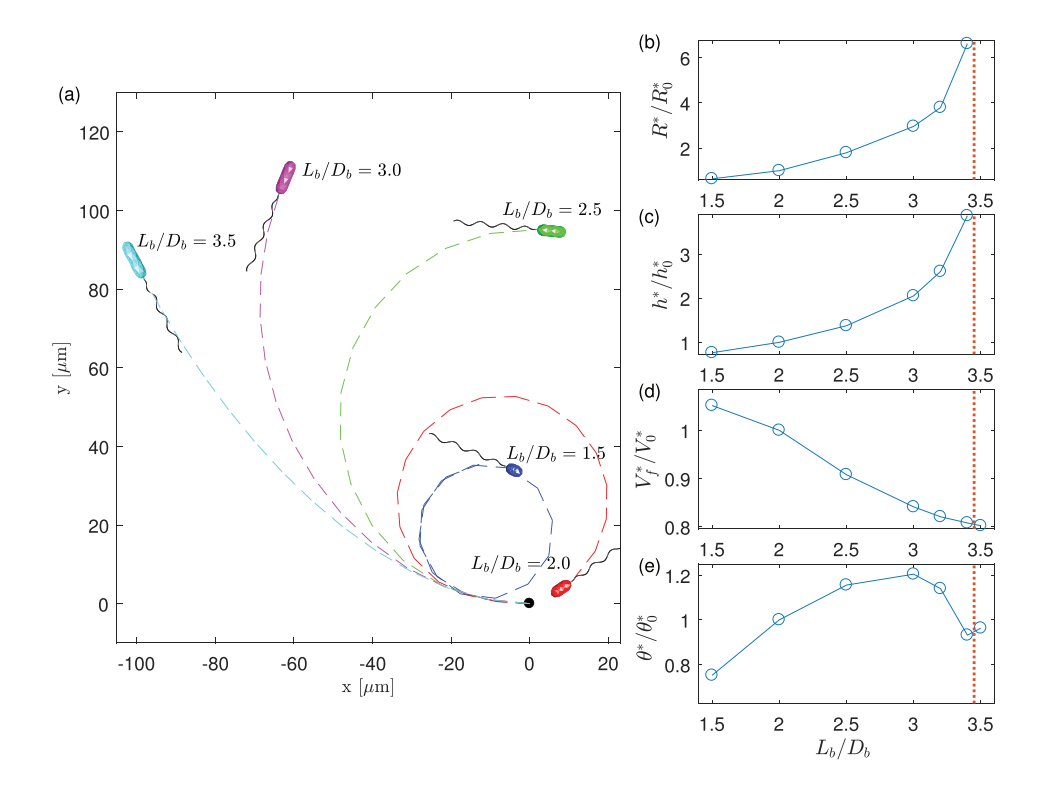


FIG. 7. Trajectories (a) of bacteria with five different aspect ratios, i.e., L_b/D_b = 1.5, 2.0, 2.5, 3.0, and 3.5, where the diameter of the body is fixed at D_b = 1.0 μ m. All bacteria are initially placed at the same location (0, 0, and 1.5 μ m) indicated by the filled circle, and the final positions of cells are captured at $t = 12.5 \,\mathrm{s}$. Normalized limiting values of radius R^*/R_0^* of curvature of the trajectory (b), height h^*/h_0^* (c), forward swimming speed V_f^*/V_0^* (d), and inclination angle θ^*/θ_0^* (e) are drawn as functions of aspect ratio L_b/D_b . The vertical dotted line in the second column indicates the threshold of the aspect ratio that separates trapping (left side) from escaping (right side) motions. Multimedia view: https://doi.org/10.1063/5.0082768.2

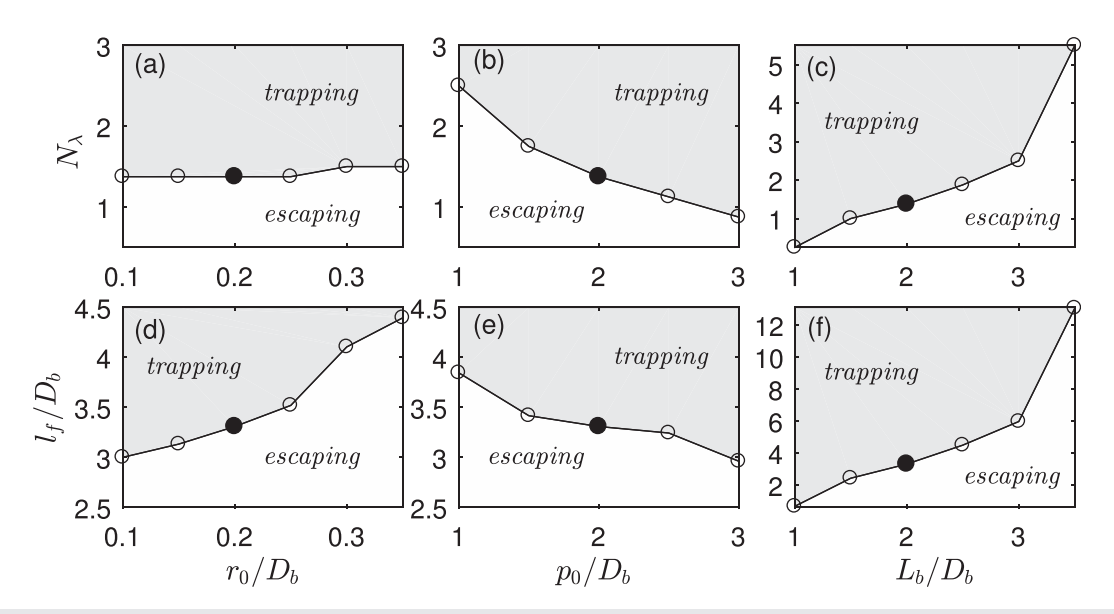


FIG. 8. Critical numbers of helical turns N_{λ} (a)–(c) and the corresponding curvilinear lengths of the flagellum I_f normalized by D_b (d)–(f) as functions of normalized helical radius r_0/D_b (a) and (d), helical pitch p_0/D_b (b) and (e), and aspect ratio L_b/D_b (c) and (f). Each curve separates the trapping zone from the escaping zone, and the filled circles represent the simulation results with the default values.

while the length of the hook being fixed at 2 Δ s. For efficient forward bacterial swimming, the hook should be as straight as possible to align well the body axis with the flagellum axis. Even though the hook stiffness is determined by the bending modulus a_1^{hook} , its proper function can be affected by the motor torque and the hook length. Thus, we consider the hook stiffness relative to the product of the motor torque τ_m with the hook length L_{h} , i.e., $a_1^{\text{hook}}/(\tau_m L_{\text{h}})$, which is called the relative hook stiffness ¹⁵

Figure 9 displays normalized limiting values of height h^*/h_0^* (a) and (b), radius R^*/R_0^* of curvature of the trajectory (c) and (d), forward swimming speed V_f^*/V_0^* (e) and (f), and inclination angle θ^*/θ_0^* (g) and (h) as functions of the relative hook stiffness, $a_1^{\text{hook}}/(\tau_m L_h)$, which is calculated with various bending moduli a_1^{hook} while L_h being fixed (left panels) and with various lengths of the hook L_h while a_1^{hook} being fixed (right panels). The filled circles represent the simulation results with the default values. Since the rotation rate of the motor is a constant at $f = 100 \,\mathrm{Hz}$, the torque τ_m generated at the motor point $\mathbf{X}(0,t)$, which is computed by $\tau_m = \mathbf{n}(0,t)\Delta s$, is approximately a constant value of 0.0021 g $\mu m^2/s^2$ in time and in all the cases considered here. We can observe that the limiting values in Fig. 9 behave in almost the same fashion as the relative hook stiffness varies even though the bending modulus of hook varies (left panels) or the length of hook varies (right panels). It is shown that the limiting values of the height h^*/h_0^* , the circular radius R^*/R_0^* , and the forward velocity V_f^*/V_0^* increase at first and then level off upon increasing relative hook stiffness. The inclination angle θ^*/θ_0^* increases first and then decreases with the maximal value at $a_1^{\rm hook}/(\tau_m L_{\rm h})=0.69$ (g) and (h). Note that, as the relative hook stiffness $a_1^{\rm hook}/(\tau_m L_{\rm h})$ decreases

Note that, as the relative hook stiffness $a_1^{\text{hook}}/(\tau_m L_h)$ decreases below 1.389, the bacterium swims more slowly (e) and (f) and more closely to the wall (a) and (b). This is related to a malfunction of the hook which is too flexible to keep the alignment of the flagellum axis to the body axis. To see this, we display in Fig. 10(a) the angle Θ

between these two axes as functions of time for three different values of $a_1^{\rm hook}/(\tau_m L_{\rm h})=1.389$ (line with "+"), 0.557 (line with "×"), and 0.463 (line with "o"). The alignment angle Θ converges to 3.14° and 7.27° for the cases with $a_1^{\rm hook}/(\tau_m L_{\rm h})=1.389$ and 0.557, respectively, i.e., the limiting alignment angle increases as the relative hook stiffness decreases. ¹⁵ A further decrement of the relative hook stiffness by lowering bending modulus or raising hook length increases the alignment angle further to induce a buckling instability in which the motor twist is not well transmitted to the flagellum. ²³ Figure 10(c) shows the configurations of the swimming bacterium with $a_1^{\rm hook}/(\tau_m L_{\rm h})=0.463$ at some selected times and illustrates the buckling of the flagellum with the alignment angle being larger than 100° as shown in (a).

After the time shown in Fig. 10(c), the simulation stops for the case with $a_1^{\rm hook}/(\tau_m L_{\rm h})=0.463$, which was also reported in Ref. 15. The reason for the stopping of simulation is that, together with the buckling instability, the bacterium goes down to and finally contact with the wall. Figure 10(b) shows time evolution of the minimum distance $d_{\rm gap}$ of the cell body from the wall normalized by the regularized parameter $\epsilon=0.105~\mu{\rm m}$. When $a_1^{\rm hook}/(\tau_m L_{\rm h})=1.389$ and 0.557, the gap converges to constant values which are smaller when the hook stiffness $a_1^{\rm hook}/(\tau_m L_{\rm h})$ is smaller. The gap decreases to be almost 0 when $a_1^{\rm hook}/(\tau_m L_{\rm h})=0.463$, which might induce the stopping of simulation.

Note also that the limiting values of h^*/h_0^* , R^*/R_0^* , V_f^*/V_0^* change only slightly even though the relative hook stiffness $a_1^{\rm hook}/(\tau_m L_{\rm h})$ changes from 1.389 to 55.6, as shown in Fig. 9. We have found that the alignment angle decreases slightly as the hook stiffness increases in this range of the hook stiffness (data not shown here). The case with $a_1^{\rm hook}/(\tau_m L_{\rm h})=55.6$ can be considered as a model without a hook which was used in Ref. 24. In the model used in Ref. 15, however, the bacterium does not swim efficiently due to a large oscillatory alignment angle when $a_1^{\rm hook}/(\tau_m L_{\rm h})\geq 2$. The difference is that the

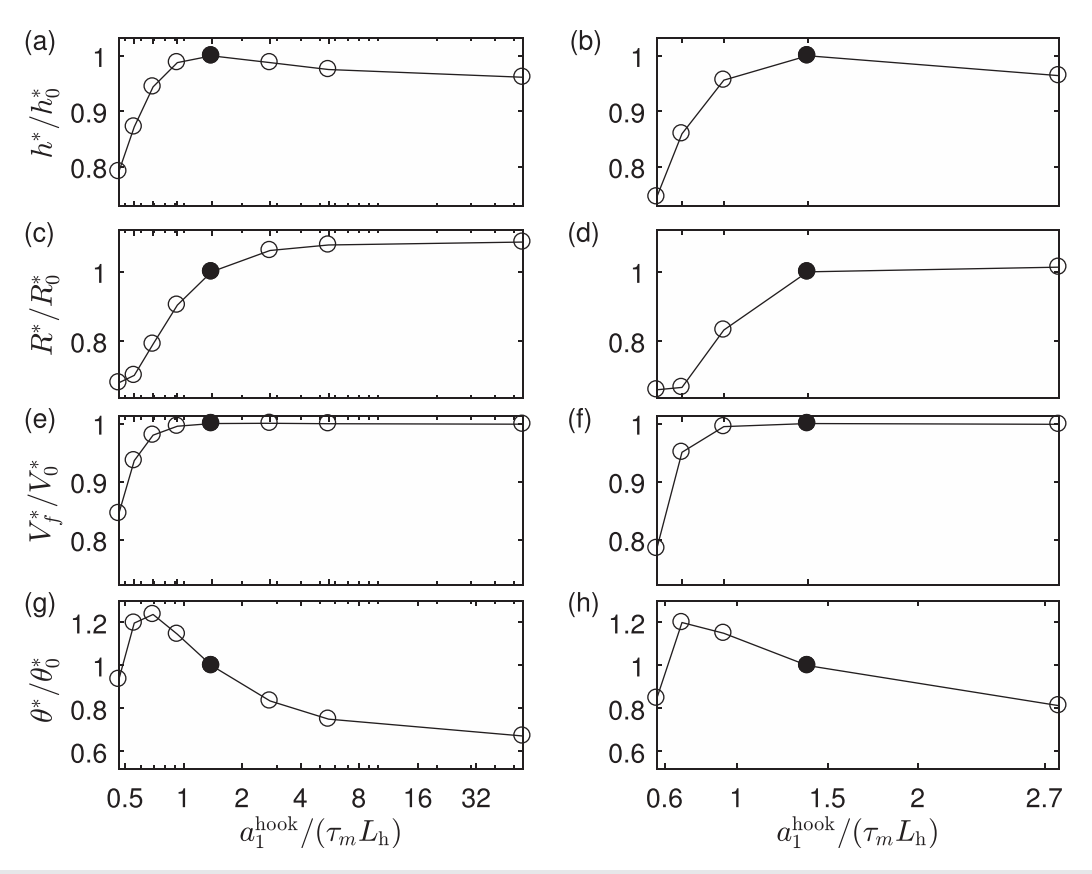


FIG. 9. Normalized limiting values of the height h^*/h_0^* (a) and (b), the radius R^*/R_0^* of curvature of the trajectory (c) and (d), the forward swimming speed V_f^*/V_0^* (e) and (f), and the inclination angle θ^*/θ_0^* (g) and (h) as functions of the relative hook stiffness, $a_1^{\text{hook}}/(\tau_m L_h)$, which is calculated with various bending moduli a_1^{hook} while L_h being fixed (left panels) and with various lengths of the hook L_h while a_1^{hook} being fixed (right panels). The motor torque is $\tau_m = 0.0021 \, \text{g} \, \mu\text{m}^2/\text{s}^2$, and the filled circles represent the simulation results with the default values.

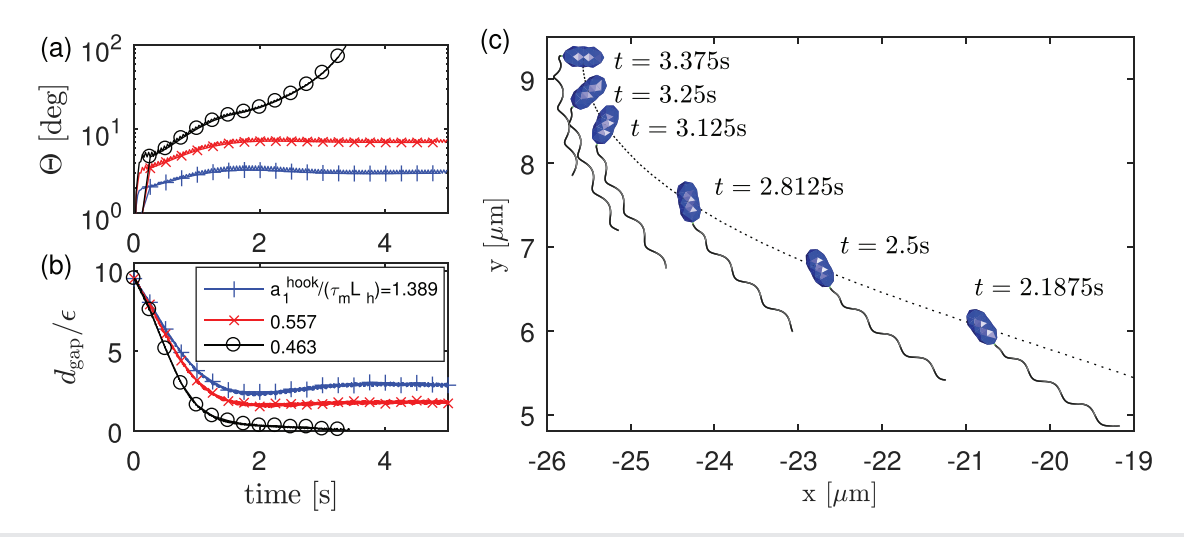


FIG. 10. Alignment angle Θ (a) between the flagellum axis and the body axis, the minimum distance $d_{\rm gap}$ (b) of the cell body from the wall normalized by the regularized parameter $\epsilon=0.105~\mu{\rm m}$ as functions of time for three different values of $a_1^{\rm hook}/(\tau_m L_{\rm h})=1.389$ (line with "+"), 0.557 (line with "**), and 0.463 (line with "o"). The configurations (c) of the swimming bacterium with $a_1^{\rm hook}/(\tau_m L_{\rm h})=0.463$ at some selected times indicate that a buckling instability occurs, in which case, the alignment angle Θ gets larger than 100° and the gap $d_{\rm gap}/\epsilon$ becomes almost 0.

hook and flagellum are both flexible in our model, while the flagellum is rigid with a flexible hook in Ref. 15.

C. Bacterial swimming dynamics in shear flow

It has been experimentally observed that a background uniform flow can alter the trajectories of bacteria near wall. The background uniform flow is in fact a shear flow in the presence of a fixed planar wall, z=0, and it can be applied by imposing on the whole domain the background velocity field of the form

$$\mathbf{u}_{\text{shear}}(\mathbf{x}) = \gamma(z, 0, 0), \tag{20}$$

where z is the z- coordinate (height) of the point \mathbf{x} , and γ is a constant representing the shear rate. This positive x-directional flow $\mathbf{u}_{\text{shear}}(\mathbf{x})$ and the associated angular velocity $\mathbf{w}_{\text{shear}}(\mathbf{x}) = \frac{1}{2}\nabla \times \mathbf{u}_{\text{shear}} = (0, \gamma/2, 0)$ are simply added to the velocities of the immersed boundaries, Eqs. (13) and (15), respectively.

Whereas a motile bacterium near a surface exhibits a circular clockwise trajectory in the absence of flow, under shear flow and noslip boundary conditions at the surface, the bacterial locomotion changes by flagellar propulsion against shear flow. Figure 11 (Multimedia view) illustrates swimming trajectories for different values of the shear rate and demonstrates that there exists a threshold of the shear rate, $\gamma_{\mathcal{O}}$ approximately 9.25/s that divides the swimming paths into two groups: periodic skewed coil paths and linear paths in the long run. Each trajectory accompanies four bacterial configurations obtained at the selected times t=0, 48 s, 51 s, and 54 s for $\gamma \leq 9$ /s and at t=0, 24, 27, and 30 s for $\gamma \geq 10$ /s.

For the values of $\gamma < \gamma_c$, the bacteria obliquely draw periodic coil trajectories and go in the direction of the shear flow $\mathbf{u}_{\text{shear}}(\mathbf{x})$ (or \mathbf{e}_1)

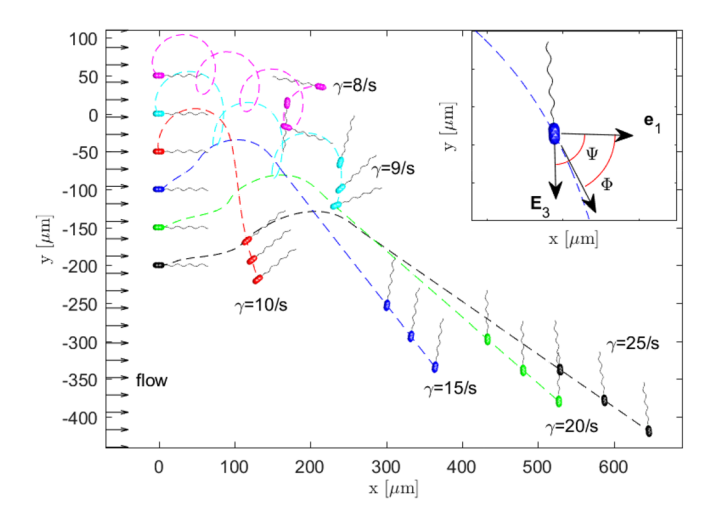


FIG. 11. Swimming trajectories of bacteria under shear flow. The shear rate is given at $\gamma=8/s,~9/s,~10/s,~15/s,~20/s,~and~25/s.$ For each trajectory, configurations of the bacterium are captured at $t=0,~48,~51,~and~54 \, s$ for $\gamma \leq 9.0/s$ and at $t=0,~24,~27,~and~30 \, s$ for $\gamma \geq 10.0/s,~and their size is enlarged by 8 times for a better visualization. The overall swimming direction of all the bacteria is in the direction of <math display="inline">e_1$ and $-e_2$; however, while the bacterium creates a coil trajectory when $\gamma \leq 9/s,~it$ draws an almost straight trajectory when $\gamma \geq 10/s.$ The inset displays the angle Ψ of the forward direction of the cell and the angle Φ of the swimming trajectory, both from the flow direction $e_1.$ Multimedia view: https://doi.org/10.1063/5.0082768.3

and also in the negative direction of the angular velocity $\mathbf{w}_{shear}(\mathbf{x})$ (or $-\mathbf{e}_2$), as observed in Refs. 35–37. These coil trajectories of the bacteria under a shear flow result in the periodic behavior of swimming properties as shown in Fig. 12, which may result from the relation between the swimming direction of the bacteria and the shear flow direction. Figure 12(a) shows time evolution of the inner product of the flow direction \mathbf{e}_1 and the forward swimming direction \mathbf{E}_3 (the unit vector from the motor point to the opposite node of the cell body) when the shear rate is $\gamma = 8.0/s$. The positive value of $\mathbf{E}_3 \cdot \mathbf{e}_1$ (gray regions) means that the bacterium swims in accord with the background flow, and its duration is shorter than that of the negative value (white regions) in which the bacterium swims against the background flow. The in-plane angle Ψ in (b), which can be computed by $\Psi = \cos^{-1}(\mathbf{E}_3 \cdot \mathbf{e}_1)$, varies periodically in time from -180° to 180° .

Figure 12 displays the normalized values of the height $h(t)/h_0^*$ (c), the radius $R(t)/R_0^*$ of curvature of the trajectory (d), and the inclination angle $\theta(t)/\theta_0^*$ (e), and the forward swimming speed $V_f(t)/V_0^*$ (f) as functions of time. The height $h(t)/h_0^*$ and the inclination angle $\theta(t)/\theta_0^*$ are in phase each other with a small phase difference but they both are in anti-phase with $E_3 \cdot e_1$. As the cell body gets well aligned with the flow (i.e., as $\mathbf{E}_3 \cdot \mathbf{e}_1$ increases), the height and inclination angle decrease, that is, the bacterium goes down with a decreasing inclination angle. As the cell body goes against the flow (i.e., as $\mathbf{E}_3 \cdot \mathbf{e}_1$ decreases), the opposite happens. The circular radius $R(t)/R_0^*$, which measures the reciprocal of the local curvature of the swimming trajectory, is generally larger when $E_3 \cdot e_1$ is positive than when it is negative. However, a large jump of the radius occurs right after the transition from the positive to negative values of $E_3 \cdot e_1$, which does not appear when $\gamma < 8/s$ (data not shown here). The forward swimming speed $V_f(t)/V_0^*$ is exactly in the same phase as $\mathbf{E}_3 \cdot \mathbf{e}_1$, which can reasonably be expected, since the forward swimming speed becomes larger as the cell body gets well aligned with the flow.

The bacterial swimming dynamics is periodic under a shear flow with $\gamma < \gamma_c$ as shown in Figs. 11 and 12 in which the period of all curves is approximately T=15.65 s when $\gamma=8/s$. Figure 13 shows the normalized period T/T_0 (a) and the angle $\tilde{\Phi}$ (b) of displacement vector of the bacteria as functions of shear rate for $\gamma < \gamma_c$. The period T is computed using the time evolution of ${\bf E}_3 \cdot {\bf e}_1$, and $T_0=12.0$ s is the period of the circular trajectory of the bacterium without shear. The angle $\tilde{\Phi}$ is the angle of the displacement vector of the bacterium over a single period from the flow direction, ${\bf e}_1$. The negative angle implies that the bacterium averagely goes to the negative y-direction, $-{\bf e}_2$. As the shear rate increases, the period T/T_0 increases but the angle $\tilde{\Phi}$ of the swimming direction decreases, i.e., the bacterium takes more time to draw one turn of the coil trajectory and moves more in the negative direction of the background angular velocity, i.e., $-{\bf e}_2$.

For the values of $\gamma > \gamma_c$, the fluid shear dominates and the behavior of the bacterium is not periodic anymore. The bacterium under a high shear flow initially tries to make a circular trajectory; however, the shear flow is so strong that the bacterium eventually swims linearly in the direction of the shear flow (e₁) and in the negative direction of background angular velocity (-e₂), see Fig. 11. Note that three configurations at times t=24 s, 27 s, and 30 s for each shear rate $\gamma \geq 10/s$ are almost parallel to one another with a certain translational distance which increases upon the increasing shear rate.

Figures 14(a) and 14(b) show time evolutions of the normalized height $h(t)/h_0^*$ (a) and two angles $\Phi(t)$ and $\Psi(t)$ (b) representing the

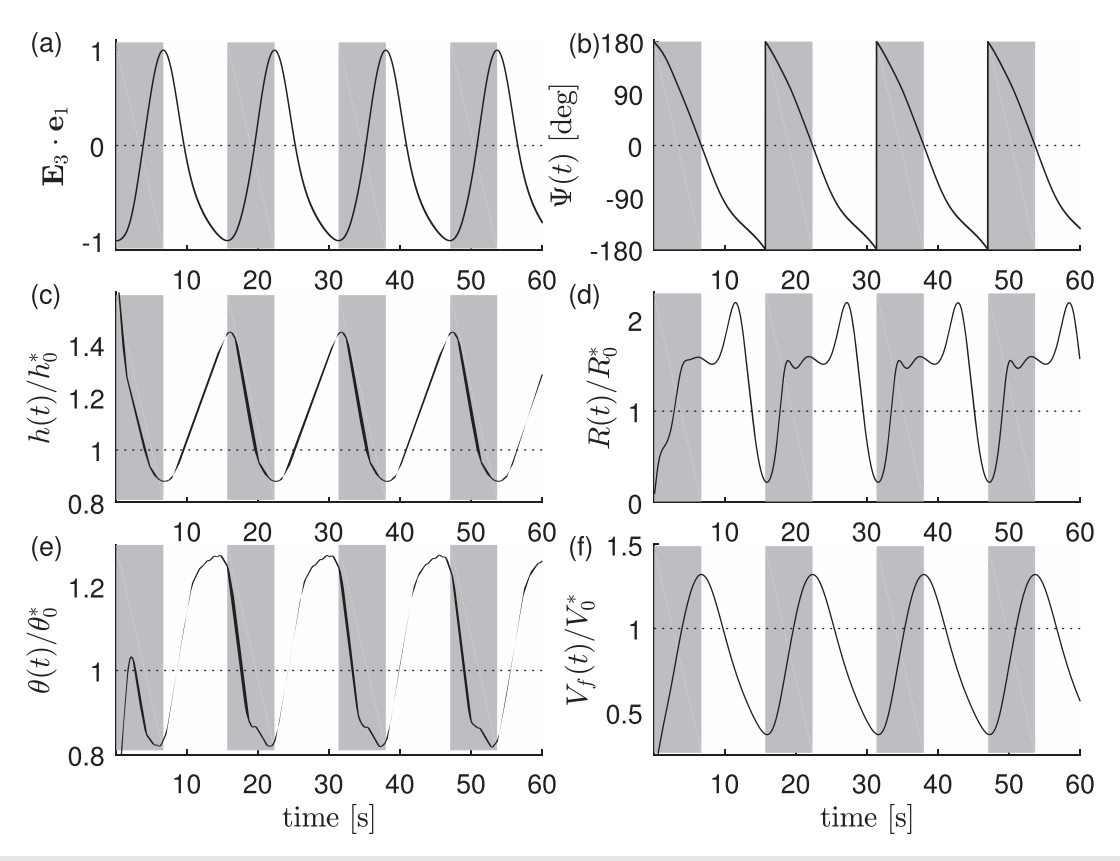


FIG. 12. Time evolutions of the inner product of \mathbf{e}_1 and \mathbf{E}_3 (a), the in-plane angle $\Psi(t)$ (b), the normalized values of the height $h(t)/h_0^*$ (c), the radius $R(t)/R_0^*$ (d), the inclination angle $\theta(t)/\theta_0^*$ (e), and the forward swimming speed $V_f(t)/V_0^*$ (f) when $\gamma=8.0$ /s. The positive (gray regions) and negative (white regions) values of $\mathbf{E}_3 \cdot \mathbf{e}_1$, respectively, represent that the bacterium swims in accord with and against the background flow. The period of all curves is approximately 15.65 s.

swimming direction of the bacterium when $\gamma=10/s$. After the bacterium goes through transient movement, the cell stays approximately at a constant height (a) and moves unidirectionally between \mathbf{e}_1 and $-\mathbf{e}_2$ with the cell pointing to a steady direction, which is indicated by the constantly negative values of $\Phi(t)$ and $\Psi(t)$ in (b).

To see more quantitatively the rheotaxis of the bacterium under a shear flow, we draw in Figs. 14(c) and 14(d) two velocity components of the cell body in the transverse direction $v_{\rm cm} = \mathbf{V}_{\rm cm} \cdot \mathbf{e}_2$ (c) and in the flow direction $u_{\rm cm} = \mathbf{V}_{\rm cm} \cdot \mathbf{e}_1$ (d), which are normalized by the swimming speed V_0^* and the instantaneous background shear flow

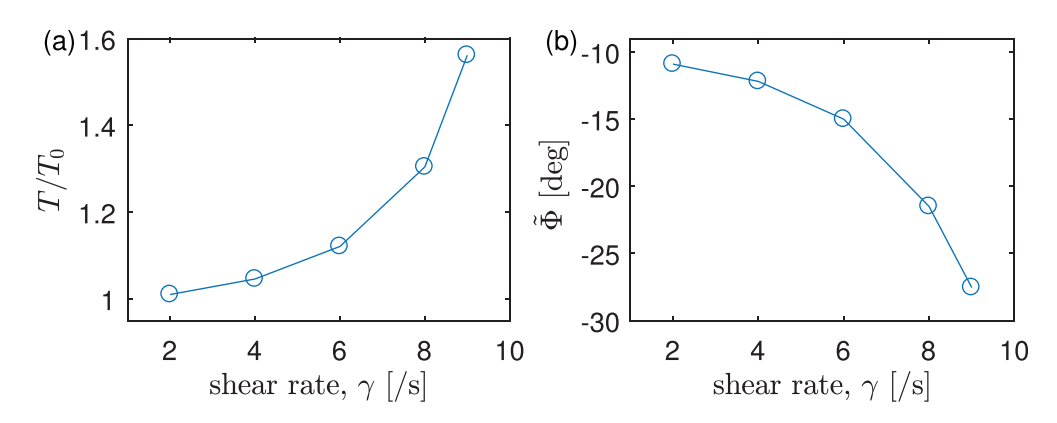


FIG. 13. Normalized period T/T_0 (a) and angle $\tilde{\Phi}$ (b) of displacement vector of the bacterium as functions of shear rate. The period T is computed using the time evolution of $\mathbf{E}_3 \cdot \mathbf{e}_1$, and $T_0 = 12.0$ s is the period of the circular trajectory of the bacterium without shear flow. The angle $\tilde{\Phi}$ of the swimming direction is the angle of the displacement vector of the bacterium over a single period from the flow direction, \mathbf{e}_1 . As the shear γ increases, the period T/T_0 increases but the angle $\tilde{\Phi}$ of the swimming direction decreases.

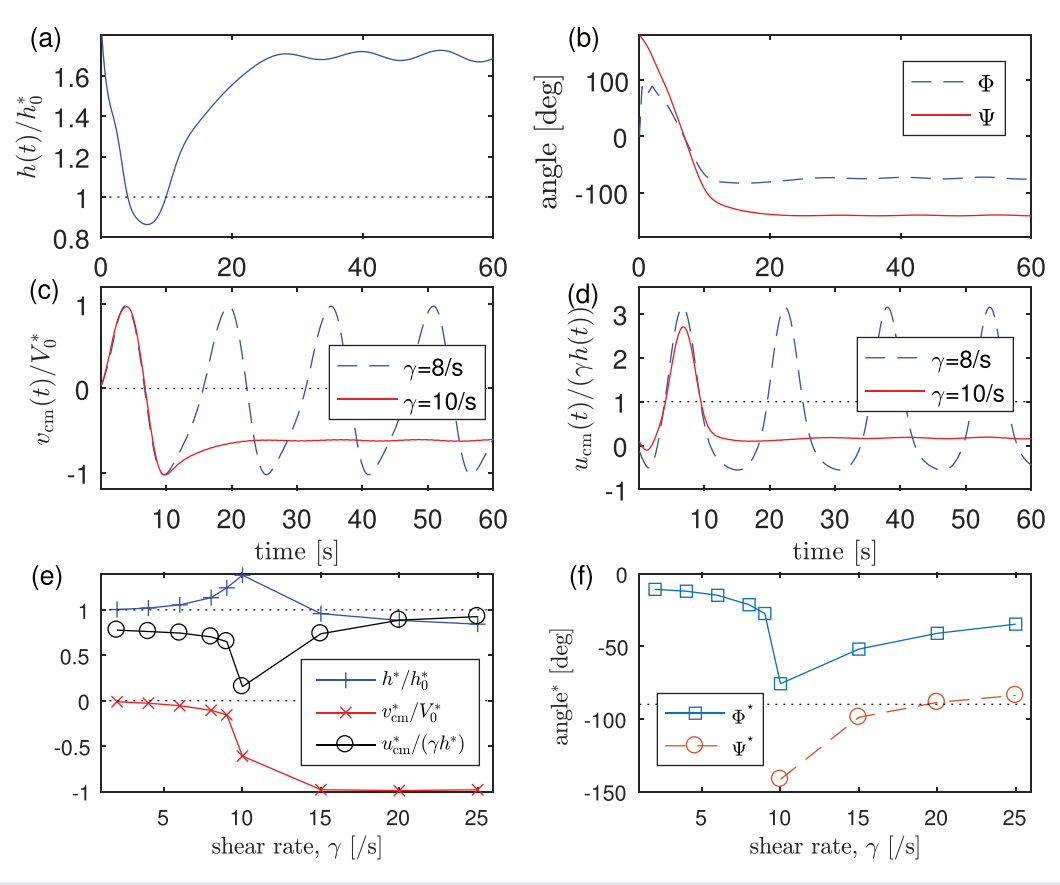


FIG. 14. Time evolutions of the normalized height $h(t)/h_0^*$ (a), and two angles $\Phi(t)$ and $\Psi(t)$ (b) when $\gamma=10$ /s. The velocity components of the cell body in the transverse direction $v_{\rm cm}=\mathbf{V}_{\rm cm}\cdot\mathbf{e}_1$ (c) and in the flow direction $u_{\rm cm}=\mathbf{V}_{\rm cm}\cdot\mathbf{e}_1$ (d), normalized by the swimming speed V_0^* and the instantaneous shear flow $\gamma h(t)$, respectively, when $\gamma=8$ /s (dashed line) and 10/s (solid line). The normalized limiting values of the height h^*/h_0^* (line with "+"), the two velocity components $v_{\rm cm}^*/V_0^*$ (line with "×") and $u_{\rm cm}^*/(\gamma h^*)$ (line with "o") of the cell body (e), and the two angles Φ^* (line with "O") (f) as functions of shear rate.

 $\gamma h(t)$, respectively. The shear rates are $\gamma=8/s$ (dashed line) and 10/s (solid line). The negative (positive) value of $v_{\rm cm}(t)/V_0^*$ indicates that the organism swims to the negative (positive) direction of background angular velocity. When $u_{\rm cm}(t)/\gamma h(t)<1$, the bacterium swims against the background flow with the instantaneous velocity $\gamma h(t)$. When $\gamma=8/s$ ($\gamma<\gamma_c$), $v_{\rm cm}(t)/V_0^*$ oscillates from -1 to 1, and $u_{\rm cm}(t)/\gamma h(t)$ varies periodically crossing the value 1. When $\gamma=10/s$ ($\gamma>\gamma_c$), after some transient time, $v_{\rm cm}(t)/V_0^*$ converges to a negative value and $u_{\rm cm}(t)/\gamma h(t)$ converges to a constant value which is less 1.

Figure 14(e) shows limiting values of the height h^*/h_0^* (line with "+"), (line with "×"), and $u_{\rm cm}^*/(\gamma h^*)$ (line with "o") as functions of the shear rate. When $\gamma < \gamma_c$, since these quantities oscillate periodically in time as shown in Figs. 12(c), 14(c), and 14(d), we average them over one period of time. As the background shear flow gets stronger, the limiting height increases first and then decreases with the maximal value at $\gamma = 10/s$. The speed $v_{\rm cm}^*/V_0^*$ in the transverse direction is all less than 0, decreasing with the increasing shear rate. The flow-directional speed $u_{\rm cm}^*/(\gamma h^*)$ is all less than 1 and decreases first and then increases with the minimal value at $\gamma = 10/s$ as the shear rate increases. We can conclude from (e) that the organism under a shear flow swims to the negative direction of background angular velocity

and against the background flow. Notice the jumps on the curves in Fig. 14(e) which indicate the separation of the swimming modes between periodic skewed coil and linear paths. Note also that, when $\gamma > 15/s$, $v_{\rm cm}^*/V_0^*$, and $u_{\rm cm}^*/(\gamma h^*)$ are close to -1 and 1, respectively. This implies that the bacterium does not only swim actively in the direction $-\mathbf{e}_2$ with its body pointing to $-\mathbf{e}_2$ but also drifts passively with the shear flow, see Fig. 11.

Figure 14(f) shows the limiting values of the angle Φ^* of the swimming direction (line with " \Box ") and the in-plane angle Ψ^* (line with " \circ ") as functions of shear rate. When $\gamma < \gamma_c$, $\Phi(t)$ and $\Psi(t)$ vary periodically from -180° to 180° , their average values over one period of time are almost 0. In this case, we draw Φ in Fig. 13(b) instead of Φ^* . As the shear flow gets stronger, while the angle Φ^* of the swimming direction gets lower first and then higher with the minimal value at $\gamma = 10/s$, the in-plane angle Ψ^* increases. It is interesting to see that, when $\gamma = 10/s$, Φ^* and Ψ^* are close to -90° (dotted line) and -150° , respectively. This indicates that the bacterium swims in the direction close to $-\mathbf{e}_2$ with the cell body pointing close to the direction of $-\mathbf{e}_1$, see Fig. 11. Figures 14(e) and 14(f) demonstrate that, under a background shear flow, the bacterium tends to move in the direction of the shear flow (\mathbf{e}_1) and in the negative direction ($-\mathbf{e}_2$) of the background angular velocity, which is consistent with the results in Refs. 34–37.

D. Upstream motility

We have observed that, when bacteria near a planar wall swim in a shear flow, they move in the direction of the shear flow and in the negative (or positive only for the case with $L_b/D_b=1.5$) direction of the background angular velocity. The experiments in Refs. 35–37, however, showed that some bacteria swim upstream in a flow channel, i.e., in the opposite direction of the flow. A possible reason for the upstream motility is the presence of physical barriers, such as side walls and some bumps on the floor around which the downstream velocity becomes small or even negative, which allows the organisms to swim against the mainstream flow.

In order to demonstrate this possibility, we construct a vertical side-wall using the target point idea. In the target point method, we impose the no-slip condition on a part of the plane $y=y_{\text{side}}$ by laying out an array of target points. We define the vertical sidewall as $\mathbf{W}_0(q,r)=(q,y_{\text{side}},r)$ for $0 \leq q \leq 14$ and $0 \leq r \leq 4.2~\mu\text{m}$, and then the target points are defined by translating $\mathbf{W}_0(q,r)$ in the x-direction by the x-coordinate of one chosen point $\mathbf{X}(s_0,t)$ of the flagellum, i.e., the target points can be written as $\mathbf{W}(q,r,t)=\mathbf{W}_0(q,r)+(\mathbf{X}(s_0,t)\cdot\mathbf{e}_1)\,\mathbf{e}_1$, see the illustrative vertical (yellow) planes in Fig. 15(b). Now letting $\mathbf{X}_w(q,r,t)$ be the corresponding moving boundary points, we impose the no-slip condition on the target wall by applying to the moving boundary $\mathbf{X}_w(q,r,t)$ the following force:

$$\mathbf{F}_{w}(q, r, t) = c_{0}(\mathbf{W}(q, r, t) - \mathbf{X}_{w}(q, r, t)),$$
 (21)

where c_0 is a large constant and $\mathbf{X}_w(q,r,t)$ moves at the local fluid velocity. This provides a feedback mechanism for computing the boundary force needed to enforce the moving boundary points $\mathbf{X}_w(q,r,t)$ to stay close to the target points $\mathbf{W}(q,r,t)$.

One might ask why we use a moving target wall instead of a large size of a fixed target wall. This is because a large size of a target wall requires to increase the number of target points (or immersed boundary points) to describe the wall with a reasonable resolution, which would make the computation for a realistic bacterial model impossible. The computational cost of our numerical method is $\mathcal{O}(N^2)$ where N is the number of immersed boundary points. Our computational model uses about 1000 immersed boundary points for the bacterium (cell body and flagellum) and 3000 target points for the small size of the moving wall. Thus, simulations of a bacterial model together with the small moving sidewall take about 16 times more computational time than the model without the sidewall.

Since the existence of the vertical sidewall in space requires the noslip boundary condition, we modify the shear flow $\mathbf{u}_{\text{shear}}(\mathbf{x})$ in Eq. (20) so that the background velocity decreases to be zero at the sidewall $y = y_{\text{side}}$. This is done by applying the shear flow of the following form:

$$\tilde{\mathbf{u}}_{shear}(\mathbf{x}) = \gamma(z g(y), 0, 0),$$

where

$$g(y) = 1 - \exp(-(y - y_{\text{side}})/10\mu\text{m}).$$
 (22)

This implies that the modified shear flow $\tilde{\mathbf{u}}_{\text{shear}}(\mathbf{x})$ is 0 at $y=y_{\text{side}}$ and increases as y increases to be close to the original shear flow $\mathbf{u}_{\text{shear}}(\mathbf{x})$ in Eq. (20). Figure 15(a) shows contours of the x-component of the shear flow $\tilde{\mathbf{u}}_{\text{shear}}(\mathbf{x})$ on a part of the imaginary (gray) plane in (b). The shear flow is 0 on the floor z=0 and on the vertical sidewall $y=-50~\mu\mathrm{m}$ and increases with z=0 and z=00, see the flow intensity values on the contours in (a). This shear flow and the background angular velocity field, which is computed by $\tilde{\mathbf{w}}_{\text{shear}}=\frac{1}{2}\,\nabla\times\tilde{\mathbf{u}}_{\text{shear}}$, are applied on the whole domain.

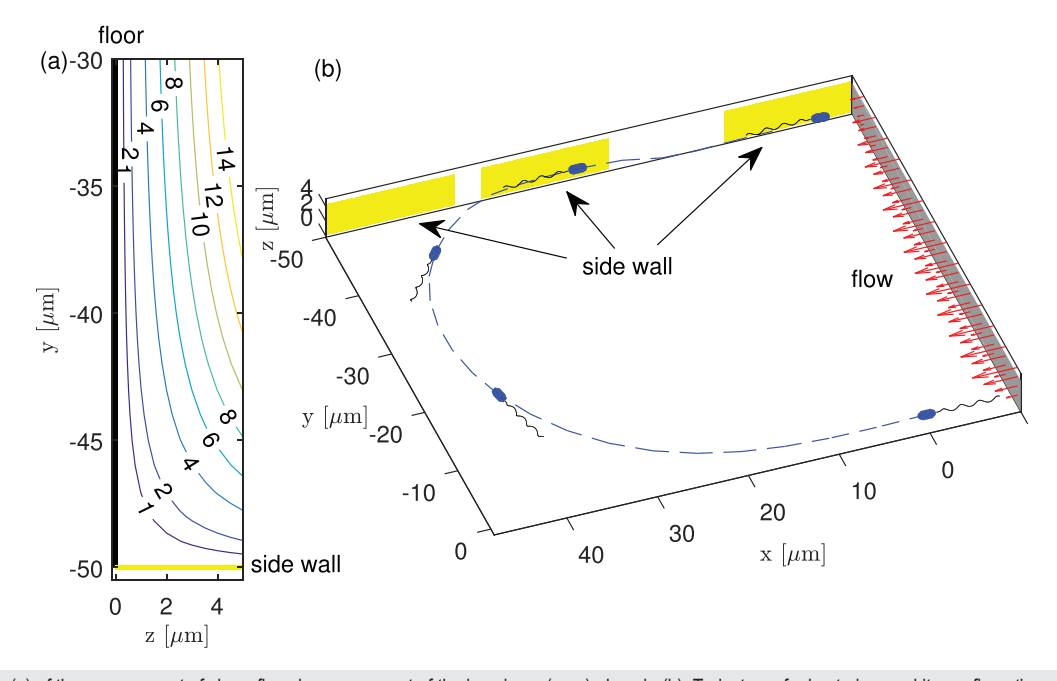


FIG. 15. Contours (a) of the *x*-component of shear flow drawn on a part of the imaginary (gray) plane in (b). Trajectory of a bacterium and its configurations are drawn at different times when there is a moving vertical sidewall (yellow planes) at $y = -50 \, \mu \text{m}$ and a background shear flow is applied on the whole domain.

Finally, in order to prevent the penetration of the immersed boundaries (cell body and flagellum) through the sidewall, we use the repulsive force $\tilde{\mathbf{f}}^r(s,t)$, which is defined as ^{59–61}

$$\tilde{\mathbf{f}}^r(s,t) = c_r \max\left(1.0 - \frac{(X_2(s,t) - y_{\text{side}})}{D_{\min}}, 0\right) \mathbf{e}_2,$$
 (23)

where c_r is a stiffness constant, \mathbf{e}_2 is the positive y-directional unit vector, $X_2(s,t)$ is the second component of the immersed boundary $\mathbf{X}(s,t)$ (flagellum and cell body), and D_{\min} is the minimum distance allowed from the sidewall to the immersed boundary. The equation says that, only when the distance from $\mathbf{X}(s,t)$ to the wall $y=y_{\text{side}}$ is less than the threshold D_{\min} , the y-directional repulsive force $\mathbf{f}^r(s,t)$ appears to act on the immersed boundary. We use $D_{\min}=0.2~\mu\mathrm{m}$ and $c_r=100~\mathrm{g}~\mu\mathrm{m}/~\mathrm{s}^2$.

Figure 16 (Multimedia view) shows swimming trajectories of four bacteria and their configurations at some selected times viewed toward the bottom wall. Each trajectory corresponds to a case with a different shear rate which is given at $\gamma=4/s$ (dotted line), 8/s (dash-dotted line), 10/s (dashed line), and 15/s (solid line), and the vertical sidewall is located at $y=-50~\mu m$. When there is no sidewall, the organism draws a periodic coiled trajectory for small shear rates and a unidirectional one for large shear rates, as shown in Fig. 11. When there is a vertical sidewall together with the horizontal bottom wall, the model organism gets close to the sidewall, turning to the opposite direction of the shear flow $(-\mathbf{e_1})$, and swims upstream, remaining close to the sidewall independent of the shear rate.

Figures 17(a) and 17(b) show time evolutions of the normalized height $h(t)/h_0^*$ (a) and the normalized distance of the cell body center from the sidewall, $(y_{\rm cm}-y_{\rm side})/D_b$ (b), for the four different shear rates: $\gamma=4/s$ (dotted line), 8/s (dash-dotted line), 10/s (dashed line), and 15/s (solid line). While the bacteria go down initially to the floor and then go up a little to reach steady states in an oscillatory manner,

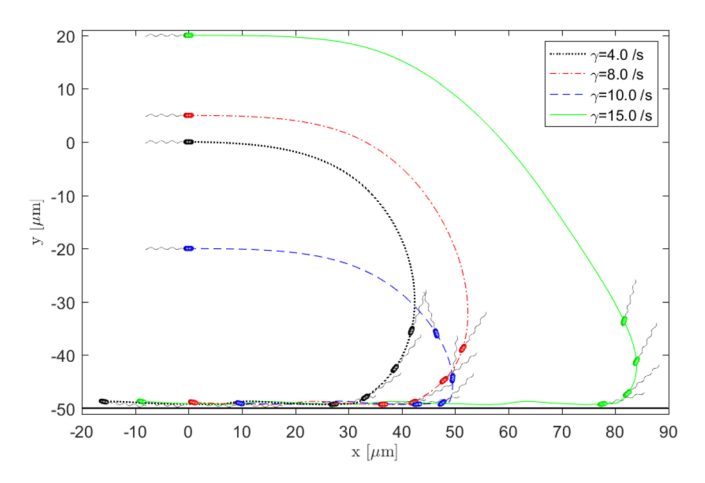


FIG. 16. Swimming trajectories and configurations of bacteria viewed toward the bottom wall at some chosen times. The shear rate is given at $\gamma=4/s$ (dotted line), 8/s (dash-dotted line), 10/s (dashed line), and 15/s (solid line), and the vertical sidewall is located at $y=-50~\mu m$. Each bacterium gets close to the sidewall, turns into the opposite direction of the shear flow $(-e_1)$, and swims upstream staying close to the sidewall independent of the shear rate. Multimedia view: https://doi.org/10.1063/5.0082768.4

they also approach the vertical sidewall initially and then oscillate around at a certain constant distance from the sidewall.

The changes of the height and the distance from the sidewall of the cell alter the magnitude of background flow, which is given in Eq. (22). Figures 17(c) and 17(d) display the x-component of normalized background shear flow at the body center, $(\tilde{\mathbf{u}}_{\text{shear}}(\mathbf{Y}_{\text{cm}}(t)) \cdot \mathbf{e}_1)/V_0^*$ (c), and the x-component of the normalized velocity of the cell body, $(\mathbf{V}_{\rm cm}(t) \cdot \mathbf{e}_1)/V_0^*$ (d), as functions of time for the four different shear rates. The background flow goes down and up initially and then decreases again to reach a steady state in an oscillatory manner. The xdirectional velocity of the cell body begins at a positive value and decreases gradually to be negative, which indicates that the bacteria swim upstream. Even though the background shear flow decreases near the floor and near the sidewall, it is still positive, as shown in (c). However, the bacteria overcome and swim against the background downstream flow. Note that $(\mathbf{V}_{\mathrm{cm}}(t)\cdot\mathbf{e}_1)/V_0^*<-1$ in the steady state in (d), which implies that the organisms swim upstream at a higher speed when there is a sidewall than when they swim without a sidewall.

We have found that the bacteria do not swim upstream in a shear flow with high shear rates. Figure 18 shows two swimming trajectories with some configurations of the bacteria viewed toward the floor at some chosen times. The shear rates are given at $\gamma=25/s$ (dash-dotted line), 30/s (dashed line), and the vertical sidewall is located at $y=-50~\mu$ m. The bacteria swim rightward ($-\mathbf{e}_2$), approach the sidewall, and turn into the upstream direction. After they move against the background downstream flow for some time, the shear flow forces them to turn again into and swim in the downstream direction. Note that the bacteria swim straight in the same direction as the background flow during the downstream swimming. This is because the bacteria escape from the region that is affected by both the bottom and side walls

IV. SUMMARY AND CONCLUSIONS

Swimming environment is important to bacterial locomotion. In this work, we present a more realistic model of a polarly flagellated bacterium and study the effect of different environmental conditions on the dynamical motion of bacteria. We consider three environmental conditions in an accumulative manner. The first condition is that there exists a horizontal rigid plane above which bacteria swim in the absence of a shear flow. The second condition is that bacteria are placed near the horizontal plane and swim under a shear flow. The last condition is that on top of the second condition there also exists a vertical plane (sidewall) that blocks the bacterial swimming through the side. Swimming behavior of bacteria changes as the environmental condition changes.

First, when the bacteria swim near the wall in the absence of shear flow, there are two types of motility—trapping and escaping motions. The trapping motion is when the bacteria stay near the surface, while the escaping motion is when the bacteria move away from the surface. In the trapping mode, the bacteria draw stable circular trajectories in which the height, the radius of curvature of the trajectory, the forward swimming speed, and the inclination angle converge to certain constant values, respectively. In the escaping mode, the bacteria escape from the trapping zone and swim freely in a linear manner and eventually there is no effect of the wall on the bacterial locomotion. These two modes are determined by the initial settings of the model

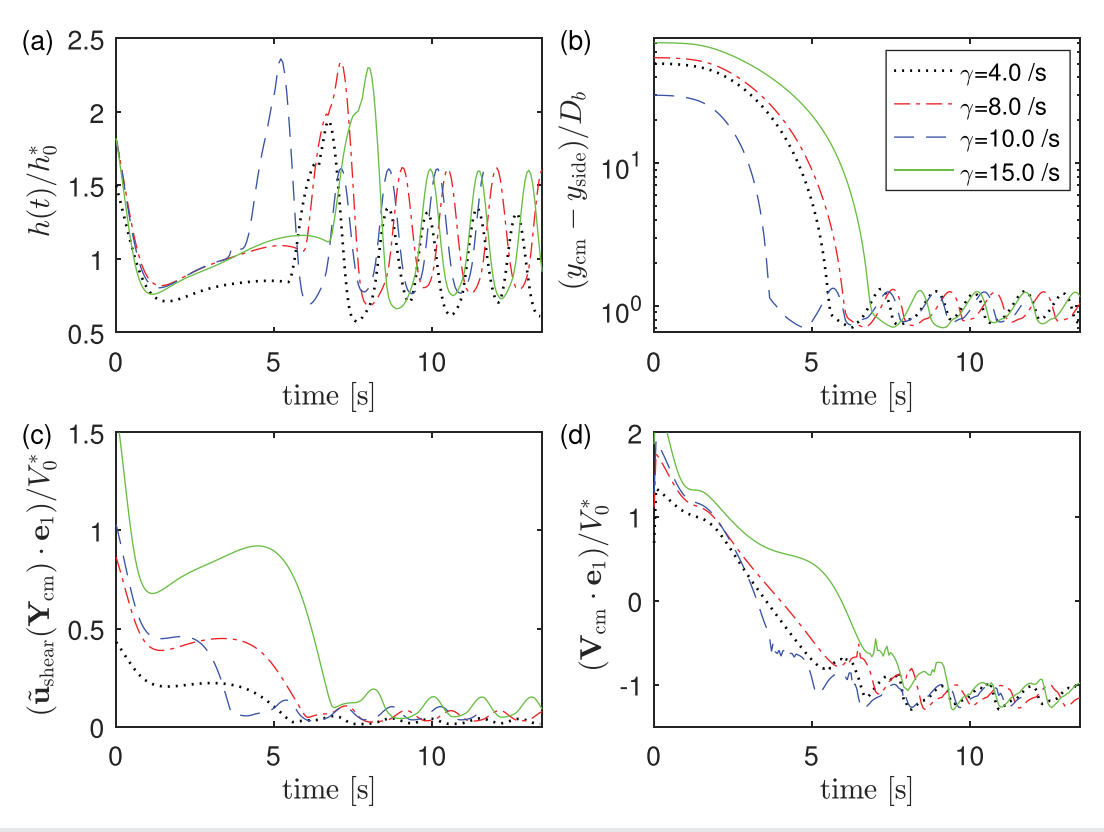


FIG. 17. Time evolutions of the normalized height $h(t)/h_0^*$ (a), the normalized distance between the cell body center and the sidewall, $(y_{cm} - y_{\text{side}})/D_b$ (b), the *x*-component of normalized background shear flow at the body center, $(\tilde{\mathbf{u}}_{\text{shear}}(\mathbf{Y}_{\text{cm}}(t)) \cdot \mathbf{e}_1)/V_0^*$ (c), and the *x*-component of the normalized velocity of the cell body, $(\mathbf{V}_{\text{cm}}(t) \cdot \mathbf{e}_1)/V_0^*$ (d), for four different shear rates: $\gamma = 4/s$ (dotted line), 8/s (dash-dotted line), 10/s (dashed line), and 15/s (solid line).

organism, such as the height of bacteria from the wall and the inclination angle of the cell body, helical properties of the flagellum, the cell body length, and the hook's properties, such as the bending modulus and the hook length. Our simulation results clearly show that the swimming motion of bacteria is sensitive to various physical parameters.

Second, when the bacterium swims near the wall and it is under the shear flow, by using the default parameters for the model bacterium, we find that there exist two types of trajectories, which are determined by the strength of the shear flow. For low shear rate, the

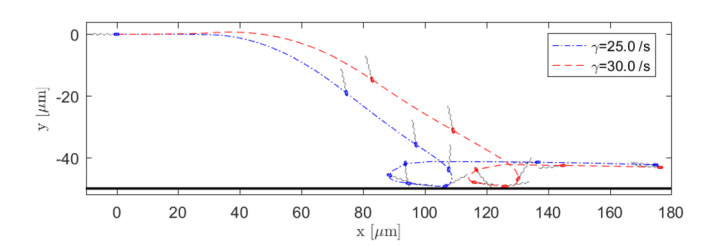


FIG. 18. Swimming trajectories and some configurations of bacteria viewed toward the floor at some chosen times. The shear rates are given at $\gamma=25/s$ (dash-dotted line), 30/s (dashed line), and the vertical sidewall is located at $y=-50~\mu\text{m}$. The bacteria swim rightward $(-e_2)$, approach the sidewall, and turn to the upstream direction. The shear flow then forces them to turn again into and swim in the downstream direction.

flagellar propulsive force is strong enough to push the bacterium against the fluid shear, and thus the bacterium draws a periodic coil trajectory while it swims rightward when viewed toward the downstream direction. It is shown that the period of the coil trajectory increases monotonically with the increasing shear rate. This implies that, as the fluid shear gets strong, the flagellar propulsive force becomes relatively weak, and the bacterium takes longer to turn the swimming direction to draw a coil trajectory. For high shear rate, the bacterium draws a linear trajectory eventually, moving rightward. Variations of geometrical properties of the bacterium can also change the overall swimming direction. For example, the bacterium with a smaller cell body length swims leftward rather than rightward when viewed toward the downstream direction.

Finally, when the bacterium is bounded by the horizontal plane together with a vertical plane and under a shear flow, we find that there exists a threshold of the shear rate that separates the upstream motility from the downstream motility. The upstream motility can be observed only when the shear rate is smaller than the critical shear rate, whereas the bacterium takes a downstream motility in the long run for larger shear rate. The upstream motility is important to study the bacterial transport in narrow passages, such as a bloodstream. Our simulations demonstrate that the passage enclosed with the horizontal and vertical planes offers the possibility of the upstream motility as long as the shear rate meets a proper condition.

There are many ways to improve the present model to be in more realistic settings, which shall be the subject of future work. With regard to the surrounding physical environment, although our model drives an upstream motility by forming a L-shaped wall with horizontal and vertical planes, bacterial movement may be altered if a bacterium is enclosed by a circular tube representing urinary tracts or blood vessels. We plan to develop an image method in a cylindrical tube to study the cell motility in the bloodstream. With regard to cell–cell interactions, cells communicate one another through quorum sensing which is a process of gene regulation in response to fluctuations in cell-population density. Quorum sensing is one of the important factors in biofilm formation, which can be incorporated into our model to study swimming behavior of bacteria.

ACKNOWLEDGMENTS

Y.K. was supported by the National Research Foundation of Korea Grant funded by the Korean Government (No. 2020R1F1A1A01074981). S.L. was supported by NSF (No. DMS-1853591), the SIMONS Foundation (No. 585683), and the Charles Phelps Taft Research Center at University of Cincinnati, USA.

AUTHOR DECLARATIONS

Conflict of Interest

The authors have no conflicts to disclose.

DATA AVAILABILITY

The data that support the findings of this study are available from the corresponding author upon reasonable request.

REFERENCES

- ¹H. C. Berg, "The rotary motor of bacterial flagella," Annu. Rev. Biochem. 72, 19–54 (2003).
- ²N. C. Darnton, L. Turner, S. Rojevsky, and H. C. Berg, "On torque and tumbling in swimming *Escherichia coli*," J. Bacteriol. 189, 1756–1764 (2007).
- ³L. Turner, W. S. Ryu, and H. C. Berg, "Real-time imaging of fluorescent flagellar filaments," J. Bacteriol 182, 2793–2801 (2000).
- ⁴H. C. Berg and L. Turner, "Chemotaxis of bacteria in glass capillary arrays. *Escherichia coli*, motility, microchannel plate, and light scattering," Biophys. J. 58, 919–930 (1990).
- ⁵P. D. Frymier, R. M. Ford, H. C. Berg, and P. T. Cummings, "Three-dimensional tracking of motile bacteria near a solid planar surface," Proc. Natl. Acad. Sci. U. S. A. 92, 6195–9199 (1995).
- ⁶M. A. S. Vigeant and R. M. Ford, "Interactions between motile *Escherichia coli* and glass in media with various ionic strengths, as observed with a three-dimensional-tracking microscope," Appl. Environ. Microbiol. **63**, 3474–3479 (1997).
- ⁷D. Giacché, T. Ishikawa, and T. Yamaguchi, "Hydrodynamic entrapment of bacteria swimming near a solid surface," Phys. Rev. E 82, 056309 (2010).
- ⁸L. A. Pratt and R. kolter, "Genetic analysis of *Escherichia coli* biofilm formation: Roles of flagella, motility, chemotaxis and type I pili," Mol. Microbiol. 30, 285–293 (1998).
- ⁹G. O'Toole, H. B. Kaplan, and R. Kolter, "Biofilm formation as microbial development," Annu. Rev. Microbiol. 54, 49–79 (2000).
- 10 R. Rusconi, S. Lecuyer, L. Guglielmini, and H. A. Stone, "Laminar flow around corners triggers the formation of biofilm streamers," J. R. Soc. Interface 7, 1293–1299 (2010).
- ¹¹N. Z. Khong, Y. Zeng, S. Lai, C. Koh, Z. Liang, K. Chiam, and H. Li, "Dynamic swimming pattern of pseudomonas aeruginosa near a vertical wall during initial attachment stages of biofilm formation," Sci. Rep. 11, 1952 (2021).

- ¹²A. J. Reynolds, "The swimming of minute organisms," J. Fluid. Mech. 23, 241–260 (1965).
- ¹³ M. Ramia, K. L. Tullock, and N. Phan-Thien, "The role of hydrodynamic interaction in the locomotion of microorganisms," Biophy. J. 65, 755–778 (1993).
- ¹⁴H. Shum, E. A. Gaffney, and D. J. Smith, "Modelling bacterial behaviour close to a no-slip plane boundary: The influence of bacterial geometry," Proc. R. Soc. A 466, 1725–1748 (2010).
- 15 H. Shum and E. A. Gaffney, "The effects of flagellar hook compliance on motility of monotrichous bacteria: A modeling study," Phys. Fluids 24, 061901 (2012)
- 16 A. Daddi-Moussa-Ider, M. Lisicki, C. Hoell, and H. Löwen, "Swimming trajectories of a three-sphere microswimmer near a wall," J. Chem. Phys. 148, 134904 (2018).
- ¹⁷D. Das and E. Lauga, "Transition to bound states for bacteria swimming near surfaces," Phys. Rev. E **100**, 043117 (2019).
- ¹⁸E. Lauga, W. R. DiLuzio, G. M. Whitesides, and H. A. Stone, "Swimming in circles: Motion of bacteria near solid boundaries," Biophys J. 90, 400–412 (2006).
- ¹⁹E. Lauga, "Bacterial hydrodynamics," Annu. Rev. Fluid Mech. 48, 105–130 (2016).
- ²⁰S. V. Srigiriraju and T. R. Powers, "Model for polymorphic transitions in bacterial flagella," Phys. Rev. E 73, 011902 (2006).
- ²¹H. Hotani, "Micro-video study of moving bacterial flagellar filaments. III. Cyclic transformation induced by mechanical force," J. Mol. Biol. 156, 791–806 (1982).
- ²²R. Vogel and H. Stark, "Rotation-induced polymorphic transitions in bacterial flagella," Phys. Rev. Lett. 110, 158104 (2013).
- ²³Y. Park, Y. Kim, and S. Lim, "Locomotion of a single-flagellated bacterium," J. Fluid Mech. 859, 586–612 (2019).
- ²⁴Y. Park, Y. Kim, and S. Lim, "Flagellated bacteria swim in circles near a rigid wall," Phys. Rev. E 100, 063112 (2019).
- ²⁵M. T. Brown, B. C. Steel, C. Silvestrin, D. A. Wilkinson, N. J. Delalez, C. N. Lumb, B. Obara, J. P. Armitage, and R. M. Berry, "Flagellar hook flexibility is essential for bundle formation in swimming *Escherichia coli* cells," J. Bacteriol. 194, 3495–3501 (2012).
- ²⁶E. E. Riley, D. Das, and E. Lauga, "Swimming of peritrichous bacteria is enabled by an elastohydrodynamic instability," Sci. Rep. 8, 10728 (2018).
- ²⁷J. S. Guasto, R. Rusconi, and R. Stocker, "Fluid mechanics of planktonic microorganisms," Annu. Rev. Fluid Mech. 44, 373 (2012).
- ²⁸N. Tufenkji, "Modeling microbial transport in porous media: Traditional approaches and recent developments," Adv. Water Resour. 30, 1455–1469 (2007)
- ²⁹K. Dohnt, M. Sauer, M. Müller, K. Atallah, M. Weidemann, P. Gronemeyer, D. Rasch, P. Tielen, and R. Krull, "An *in vitro* urinary tract catheter system to investigate biofilm development in catheter-associated urinary tract infections," J. Microbiol. Methods 87, 302–308 (2011).
- ³⁰J. R. Taylor and R. Stocker, "Trade-offs of chemotactic foraging in turbulent water," Science 338, 675-679 (2012).
- ³¹J. W. Costerton, P. S. Stewart, and E. P. Greenberg, "Bacterial biofilms: A common cause of persistent infections," Science 284, 1318–1322 (1999).
- ³²C. von Eiff, B. Jansen, W. Kohnen, and K. Becker, "Infections associated with medical devices: Pathogenesis, management and prophylaxis," Drugs 65, 179–214 (2005).
- 33R. Bain, R. Cronk, R. Hossain, S. Bonjour, K. Onda, J. Wright, H. Yang, T. Slaymaker, P. Hunter, A. Prüss-Ustün, and J. Bartram, "Global assessment of exposure to faecal contamination through drinking water based on a systematic review," Trop. Med. Int. Health 19, 917–927 (2014).
- ³⁴G. Jing, A. Zöttl, É. Clément, and A. Lindner, "Chirality-induced bacterial rheotaxis in bulk shear flows," Sci. Adv. 6, eabb2012 (2020).
- 35J. Hill, O. Kalkanci, J. L. McMurry, and H. Koser, "Hydrodynamic surface interactions enable *Escherichia coli* to seek efficient routes to swim upstream," Phys. Rev. Lett. 98, 068101 (2007).
- 36T. Kaya and H. Koser, "Direct upstream motility in Escherichia coli," Biophys. J. 102, 1514—1523 (2012).
- ³⁷A. Mathijssen, N. Figueroa-Morales, G. Junot, É. Clément, A. Lindner, and A. Zöttl, "Oscillatory surface rheotaxis of swimming E. coli bacteria," Nat. Commun. 10, 3434 (2019).

- ³⁸R. Rusconi, J. S. Guasto, and R. Stocker, "Bacterial transport suppressed by fluid shear," Nat. Phys. 10, 212–217 (2014).
- ⁵⁹G. B. Jeffery, "Ellipsoidal particles immersed in a viscous fluid," Proc. R. Soc. Lond. A 102, 161–179 (1922).
- ⁴⁰F. P. Bretherton, "The motion of rigid particles in a shear flow at low Reynolds number," J. Fluid Mech. 14, 284–304 (1962).
- ⁴¹A. Zöttl and H. Stark, "Nonlinear dynamics of a microswimmer in Poiseuille flow," Phys. Rev. Lett. 108, 218104 (2012).
- ⁴²A. Zöttl and H. Stark, "Periodic and quasiperiodic motion of an elongated microswimmer in poiseuille flow," Eur. Phys. J. E 36, 4 (2013).
- ⁴³G. Junot, N. Figueroa-Morales, T. Darnige, A. Lindner, R. Soto, H. Auradou, and E. Clément, "Swimming bacteria in Poiseuille flow: The quest for active Bretherton-Jeffery trajectories," Europhys. Lett. 126, 44003 (2019).
- ⁴⁴Marcos, H. C. Fu, T. R. Powers, and R. Stocker, "Bacterial rheotaxis," Proc. Natl. Acad. Sci. U. S. A. 109, 4780–4785 (2012).
- ⁴⁵N. Figueroa-Morales, G. L. Minö, A. Rivera, R. Caballero, E. Clément, E. Altshulerb, and A. Lindner, "Living on the edge: Transfer and traffic of *E. coli* in a confined flow," Soft Matter 11, 6284–6293 (2015).
- ⁴⁶R. Baker, J. E. Kauffman, A. Laskar, O. E. Shklyaev, M. Potomkin, L. D.-R. adn, H. Shum, Y. Cruz-Rivera, I. S. Aranson, A. C. Balazs, and A. Sen, "Fight the flow: The role of shear in artificial rheotaxis for individual and collective motion," Nanoscale 11, 10944–10951 (2019).
- ⁴⁷C. Brosseau, F. B. Usabiaga, E. Lushi, Y. Wu, L. Ristroph, J. Zhang, M. Ward, and M. J. Shelley, "Relating rheotaxis and hydrodynamic actuation using asymmetric gold-platinum phoretic rods," Phys. Rev. Lett. 123, 178004 (2019).
- ⁴⁸Y. Kim and C. S. Peskin, "A penalty immersed boundary method for a rigid body in fluid," Phys. Fluids 28, 033603 (2016).
- ⁴⁹S. Lim, A. Ferent, X. S. Wang, and C. S. Peskin, "Dynamics of a closed rod with twist and bend in fluid," SIAM J. Sci. Comput. 31, 273–302 (2008).

- 50S. Olson, S. Lim, and R. Cortez, "Modeling the dynamics of an elastic rod with intrinsic curvature and twist using a regularized Stokes formulation," J. Comput. Phys. 238, 169–187 (2013).
- ⁵¹J. Ainley, S. Durkin, R. Embid, P. Boindala, and R. Cortez, "The method of images for regularized stokeslets," J. Comput. Phys. 227, 4600–4616 (2008).
- 52R. Cortez and D. Varela, "A general system of images for regularized Stokeslets and other elements near a plane wall," J. Comput. Phys. 285, 41–54 (2015).
- 53Y. Kim and C. S. Peskin, "Penalty immersed boundary method for an elastic boundary with mass," Phys. Fluids 19, 053103 (2007).
- ⁵⁴J. J. Higdon, "The hydrodynamics of flagellar propulsion: Helical waves," J. Fluid Mech. **94**, 331–351 (1979).
- 55R. Cortez, "The method of regularized Stokeslets in three dimensions: Analysis, validation, and application to helical swimming," Phys. Fluids 17, 031504 (2005)
- ⁵⁶S. Kudo, N. Imai, M. Nishitoba, S. Sugiyama, and Y. Magariyama, "Asymmetric swimming pattern of *vibrio alginolyticus* cells with single polar flagella," FEMS Microbiol. Lett. **242**, 221–225 (2005).
- 57Y. Magariyama, M. Ichiba, K. Nakata, K. Baba, T. Ohtani, S. Kudo, and T. Goto, "Difference in bacterial motion between forward and backward swimming caused by the wall effect," Biophys. J. 88, 3648–3658 (2005).
- 58J. R. Blake, "A note on the image system for a stokeslet in a no-slip boundary," Math. Proc. Cambridge Philos. Soc. 70, 303–310 (1971).
- ⁵⁹G. Chirico and J. Langowski, "Brownian dynamics simulations of supercoiled dna with bent sequences," Biophys. J. 71, 955–971 (1996).
- ⁶⁰S. Lim, Y. Kim, and D. Swigon, "Dynamics of an electrostatically charged elastic rod in fluid," Proc. R. Soc. 467, 569–590 (2011).
- ⁶¹J. R. Banavar, O. Gonzalez, J. H. Maddocks, and A. Maritan, "Self-interactions of strands and sheets," J. Stat. Phys 110, 35–50 (2003).